Journal of Geochemical Exploration 204 (2019) 256–269

Contents lists available at ScienceDirect

Journal of Geochemical Exploration

journal homepage: www.elsevier.com/locate/gexplo

Geochemical attributes of magmatic apatite in the Kukaazi granite from western Kunlun orogenic belt, NW China: Implications for granite petrogenesis and Pb-Zn (-Cu-W) mineralization

Tehseen Zafar[a,c], Cheng-Biao Leng[a,b,*], Xing-Chun Zhang[a], Hafiz Ur Rehman[d]

[a] State Key Laboratory of Ore Deposit Geochemistry, Institute of Geochemistry, Chinese Academy of Sciences, Guiyang 550081, China
[b] State Key Laboratory of Nuclear Resources and Environment, East China University of Technology, Nanchang 330013, China
[c] University of Chinese Academy of Sciences, Beijing 100049, China
[d] Department of Earth and Environmental Sciences, Kagoshima University, Kagoshima, Japan

ARTICLE INFO

Keywords:
Magmatic apatite
Kukaazi deposit
Rare earth elements (REEs)
Adakite
Moderate oxidation state
Petrogenetic attributes

ABSTRACT

Apatite is a significant accessory mineral which is ubiquitous in Kukaazi granitic bodies and provides vital geological information concerning petrogenetic as well as metallogenic attributes. Particularly, igneous apatite is important to delineate nature of parental magma and its characteristics. Here we present new EPMA and LA-ICP-MS data on magmatic apatite of Kukaazi pluton to explore its potential in petrogenesis as well as mineralization and this deposit is widely exposed in western Kunlun, NW China. Our results reveal that the apatite can be characterized as fluorapatite and it reflects the parental magma characteristics of Kukaazi granite. The apatite exhibits high fluorine content, right inclined distribution pattern with enrichment of light rare earth elements (LREEs), a prominent moderate negative Eu anomaly and this anomaly is possibly resulting from plagioclase crystallization prior to apatite. The negative correlation and variation of δCe and δEu together with the moderate negative Eu anomaly suggests that the parental magma of Kukaazi granite have moderate oxidizing nature. The apatite also reveals Kukaazi pluton with adakitic affinity containing higher Sr/Y and Eu/Eu* ratios. This implies that the fluorapatite can be robust tool for distinguishing the adakite plutons and may preserve original Sr/Y and Eu/Eu* ratios as a result of no influence of hydrothermal alteration. Our results also indicate that apatite Cl/F ratio is a potential indicator to track the content of magmatic volatiles and pointer for mineralization. It is inferred that Cl/F ratio in the parental magma of Kukaazi pluton is low, attributable to source control and discrepancy in the Cl/F values can be ascribed to variability of degassing. Halogen data indicates low Cl, fairly high F and low Cl/F ratios which implies that the parental magma of Kukaazi granite is produced in consequence of partial melting of lower crust material. The negative correlation of F and Cl suggests crystallization of Kukaazi apatite from hydrous parental magma. Besides, apatite Eu/Eu* vs. Cl content is significant as proxy record to discriminate mineralized rock from unmineralized. Based on Eu/Eu* vs. Cl plot, we propose that the Kukaazi granite is mineralized. Furthermore, variation and positive correlation between F/Cl ratios and F contents, increase in fluorine concentration, (La/Yb) N and δEu possibly support process of magmatic differentiation. Based on apatite geochemistry, we identified two types of ore deposits specifically Mo-W and Cu deposit in Kukaazi area. In comparison, the apatite of Mo-W deposit is distinguished by slightly higher fluorine and Y, lesser Sr and δEu values however, copper deposits are characterized by higher Sr, δEu values and lesser F, Y. These elements of apatite are prime prolific indicators and proxies for distinguishing fertile granite from barren one. Thus, in view of these findings, we confirm that apatite is a potential pointer of petrogenesis, metallogenesis, mineralization and ore varieties.

1. Introduction

Apatite is significant accessory mineral that is omnipresent in granitic bodies and reflected as one of the leading repository for volatiles, rare earth elements, phosphorus, strontium and notable quantities of uranium and thorium (Nagasawa, 1970; Henerson, 1980; Wass et al., 1980; Roeder et al., 1987; Ayers and Watson, 1993; Warner et al., 1998; Pan and Fleet, 2002; Piccoli and Candela, 2002; Chen and

* Corresponding author at: State Key Laboratory of Ore Deposit Geochemistry, Institute of Geochemistry, Chinese Academy of Sciences, Guiyang 550081, China.
E-mail address: lengchengbiao@vip.gyig.ac.cn (C.-B. Leng).

https://doi.org/10.1016/j.gexplo.2019.06.005
Received 16 January 2019; Received in revised form 6 April 2019; Accepted 20 June 2019
Available online 21 June 2019
0375-6742/

Simonetti, 2014; Webster and Piccoli, 2015). Apatite crystallizes from melts (Watson, 1980; Harrison and Watson, 1984; Jahnke, 1984; Pichavant et al., 1992; Wolf and London, 1994; London et al., 1999), and during metamorphic as well as hydrothermal activity, the ingredients of apatite remain extremely stable (Ekstrom, 1972; Ayers and Watson, 1991; Creaser and Gray, 1992). In view of its durability not prone to hydrothermal and metamorphic actions (Ayers and Watson, 1991; Creaser and Gray, 1992; Bouzari et al., 2011), magmatic apatite can possibly track and conserve facts regarding nature of its parental magma (Webster and Piccoli, 2015). Hence, it can sustain vital geological data concerning crystallization process, which is essential to regulate the volatile components and source of the melt (Mathez and Webster, 2005; Marks et al., 2012; Scott et al., 2015; Pan et al., 2016; Chakhmouradian et al., 2017; Mitchell et al., 2017).

Nominally, this important mineral accommodates much of the periodic table into its lattice, making it valuable tool for an extensive range of geochemical approach (Farley and Stockli, 2002; Gleadow et al., 2002; Pan and Fleet, 2002; Pyle et al., 2001; Spear and Pyle, 2002; Hovis et al., 2007; Schoene and Bowring, 2007; Hughes and Rakovan, 2015). Owing to numerous substitutions in its structure, apatite hosts various elements and therefore can be used to investigate magmatic evolutionary processes (Ishihara, 1981; Korzhinskiy, 1981; Nash, 1984; Hsieh et al., 2008; Chu et al., 2009), radiometric and fission track dating (Zeitler et al., 1987; McInnes et al., 1999; Farley and Stockli, 2002; Harrison et al., 2002; Omar et al., 1987; Gleadow et al., 2002; Hasebe et al., 2004), compositional assessment of chloride and fluoride, halogen fugacity evaluation (Korzhinskiy, 1981; Zhu and Sverjensky, 1992), geochemical prospecting (Treloar and Colley, 1996; Belousova et al., 2001, 2002) and temperature estimation (Munoz, 1984; Sallet, 2000). Furthermore, apatite can assist as a striking tool and suitable probe to deduce characteristics of fluids, for instance, the development of volatiles (Piccoli and Candela, 1994; Streck and Dilles, 1998; Van Hoose et al., 2013; Scott et al., 2015), inferences for the type of linked ore deposits (Krneta et al., 2016), rock formation (Sha and Chappell, 1999; Belousova et al., 2001; Chu et al., 2009; Cao et al., 2012; Pan et al., 2016), mineral exploration and formation of magmatic deposits (Harlov et al., 2002; Bonyadi et al., 2011; Cao et al., 2012; Pan et al., 2016; Mao et al., 2016; Chen et al., 2017) as well as magma oxidation (Miles et al., 2014; Pan et al., 2016). Certain elements in apatite including Mn, Sr, LREE, Th, Y, Eu and Ce can be applicable to infer the magma compositions in addition to reductive state and oxidation condition of the parental magma (Miles et al., 2014; Cao et al., 2012; Belousova et al., 2001, 2002; Piccoli and Candela, 2002; Sha and Chappell, 1999; Tepper and Kuehner, 1999). Moreover, the magmatic volatiles in apatite such as F, Cl, S and C depict substantial character to clarify the magma volatile constituents and to delineate petrogenetic processes (Bruand et al., 2017; Miles et al., 2014; Parat et al., 2011). These volatiles provide prime inferences for the migration and precipitation of several metals (Harris et al., 2004; Williams–Jones and Heinrich, 2005; Cao et al., 2012; Scott et al., 2015; Mao et al., 2016; Pan et al., 2016; Chen et al., 2017).

Few researchers have deliberated apatite as important pointer for metallogenesis and magma characteristics (Belousova et al., 2001, 2002; Imai, 2002, 2004; Cao et al., 2012; Pan et al., 2016). In view of the exclusive properties of apatite, the composition of apatite is very vital to attain a better conception regarding petrogenesis and metallogenesis of various ore deposits. Hence, to assess its pertinence and inspect some inferences, we have designated apatite-bearing Kukaazi Ordovician granites with diverse mineralization of Pb-Zn-Cu-W, exposed in Western Kunlun orogenic belt, NW China. The Kukaazi distal skarn deposit is well-exposed in the western Kunlun orogenic belt between the Tarim Craton and the Karakorum–Qiangtang Block (Fig. 1a; Xu et al., 2011; Zhang et al., 2015). A number of huge to massive polymetallic deposits containing Pb–Zn–Cu and W have been documented in this area, making it the prime emphasis for mineralization exploration (Sun et al., 2003; Z.W. Zhang et al., 2014; Leng et al., 2018). Numerous researchers have explored these giant deposits, principally focusing on their geological settings, geochemical evolution and metallogenic character (Mattern and Schneider, 2000; Xiao et al., 2002, 2005; Xu et al., 2011; C. Wang et al., 2013; Y.H. Wang et al., 2013; Zhang et al., 2015; Liu et al., 2016; Leng et al., 2018) however, no investigation has been conducted in terms of constituent mineral of the ore-forming rock such as apatite, its origin and metallogenic specificity. This motivated the authors to investigate apatite geochemistry and to explore its applications for petrogenesis and mineralization potential of Kukaazi granites. On the basis of geochemical analysis, we recognize the presence of apatite in scanning electron microscope (SEM) and use electron probe micro-analyzer (EPMA) for major elements evaluation and laser ablation inductively coupled plasma mass spectrometry (LA-ICP-MS) for determination of minor/trace elements. The obtained new geochemical data is interpreted here to investigate the geochemical characteristics of various elements in apatite and to suggest a methodical enlightenment on petrogenetic significance. With these data we attempt to appraise the functionality of apatite in petrogenesis and mineralization assessment by answering the following questions: (1) To what degree does magmatic apatite reflect the parental magma characteristics of Kukaazi granite? And (2) Can apatite chemical composition be used as proxy to pinpoint mineralization potential and regional metallogeny of Kukaazi pluton? The outcomes and goals of our research stated in this paper substantiate that apatite is not only a consistent petrogenetic pointer but also a valuable exploration tool. In addition, we expect that the present research can deliver an avenue for further study regarding metallogenic potential, ore types, apatite origin and magmatic characteristics using apatite geochemistry.

2. Geological setting

The Kukaazi deposit is well exposed between the Tarim Craton and the Karakorum-Qiangtang Block and tectonically it is present in domain of western Kunlun orogenic belt (Fig. 1a; Xu et al., 2011; Zhang et al., 2015). The structural framework in this area is considered as narrow structural belt in NW-SE-trend. Previous studies demonstrated that the western Kunlun orogenic belt can be alienated into three terranes including the Taxkorgan-Tianshuihai, northern and the southern Kunlun, respectively (Fig. 1b). From north to south, these terranes are bounded through the Akazi-Kegang and the Mazha-Kangxiwa Fault, correspondingly (Pan, 1989; Mattern et al., 1996; Mattern and Schneider, 2000; Xiao et al., 2002; Zhang et al., 2015). The North Kunlun Terrane was reflected to be a segment of the Tarim Craton and restricted through the faults specifically Tiekelike and Akazi-Kegang Fault (Pan et al., 1994; Xu et al., 1994; Jiang et al., 2000; Yuan et al., 2003). This region is primarily comprised of the Proterozoic to Lower Paleozoic metamorphosed bodies, which are superimposed via Devonian to Triassic terrigenous and carbonate rocks (Xiao et al., 2002). Prior researches proposed that the metamorphosed basement of the North Kunlun Terrane was possibly developed in the age of 2.4–0.8 Ga (Zhang et al., 2004, 2007; Wang et al., 2009). On the other hand, the South Kunlun Terrane is exposed predominantly between the Mazha-Kangxiwa and Akazi-Kegang faults and it is represented by the presence of variable lithologies particularly Kudi ophiolites and Precambrian gneiss schist-migmatite complex (Yin and Harrison, 2000; Xiao et al., 2002). However, its southern portion is characterized by existence of plutonic rocks having Early Carboniferous to Late Triassic ages (Xiao et al., 2002). The rocks of the North Kunlun Terrane reveal (2.8 Ga) depleted mantle Nd model age which is comparatively older to Precambrian rocks of the South Kunlun demonstrating (1.5–1.1 Ga; Yuan et al., 2002). Furthermore, by high-precision SHRIMP technique, the zircon U-Pb dating of the Kudi ophiolite assemblage was evaluated between 525 and 510 Ma (Xiao et al., 2003; Zhang et al., 2004). In terms of lithological assemblages, the Taxkorgan-Tianshuihai Terrane comprises sequence of flysch-facies representing Permo-Triassic ages (Mattern et al., 1996). This terrane was developed owing to northward

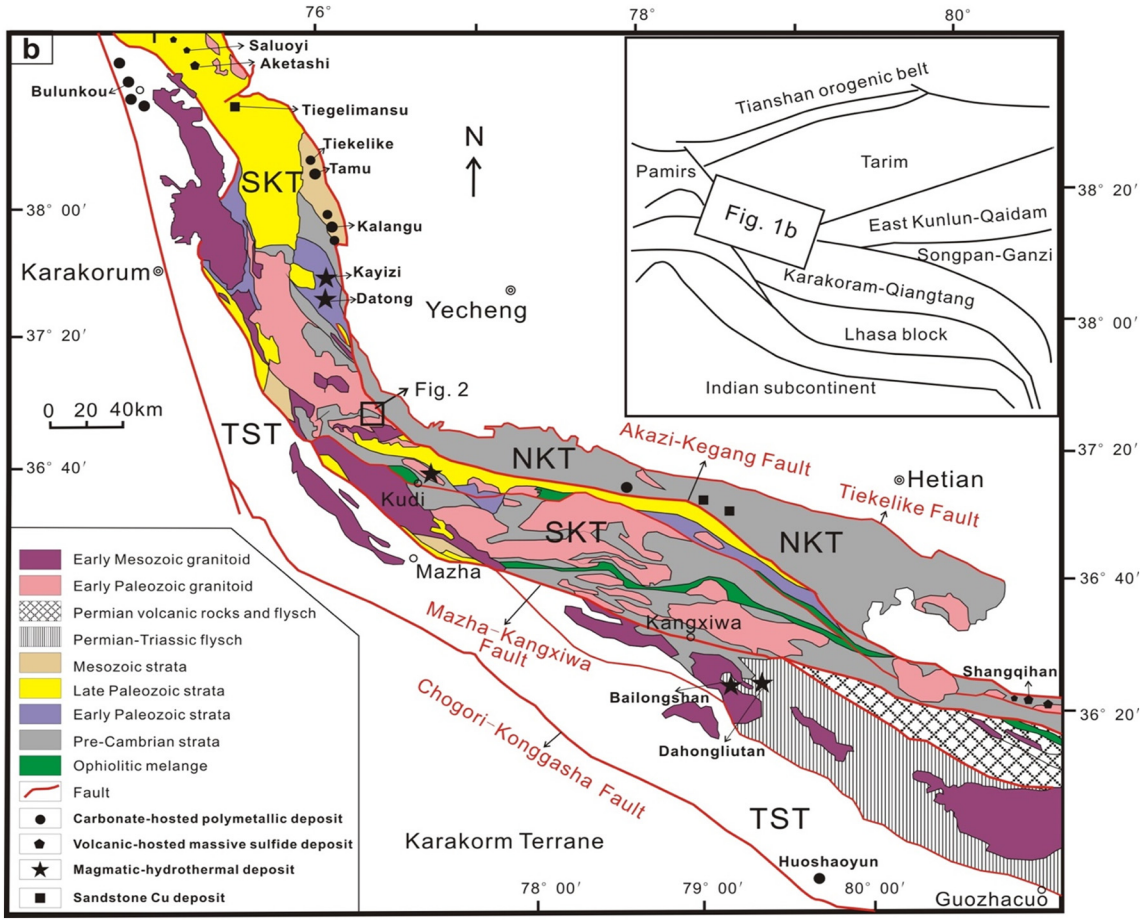

Fig. 1. a, b Geologic map of the western Kunlun and its adjoining areas showing location of Kukaazi and characteristic metallic deposits (modified after Leng et al., 2018).

convergence of the Paleo-Tethyan oceanic basin and pondered as massive accretionary wedge (Xiao et al., 2005). The Western Kunlun orogenic belt had subjected Proto to Paleo-Tethyan oceans progression in Early Paleozoic to Triassic (Pan et al., 1994; Mattern et al., 1996; Mattern and Schneider, 2000; Xiao et al., 2002, 2005; Xu et al., 2015; Zhang et al., 2015). Widespread granitic rocks were emplaced in this orogenic belt in consequence of expansion, convergence and termination of the diverse phases of Tethyan oceanic basins (Fig. 1b; C. Wang et al., 2013; Zhang et al., 2015). The Early Paleozoic granite subsequently intruded the metamorphic basement rocks during 521 to 431 Ma and these intrusions are dispersed mostly in the northern and southern Kunlun (Fig. 1b; Zhang and Xie, 1989; Fang and Wang, 1990; Xu et al., 1994; Jiang et al., 1999, 2000; Yuan et al., 2003; Cui et al., 2006, 2007; Yu et al., 2011; C. Wang et al., 2013). These granites are proposed to be generated as a result of partial melting of mafic lower crust in active continental arc and display arc characteristics (Yuan et al., 2003; C. Wang et al., 2013; Jia, 2013). In addition, along Mazha-Kangxiwa Fault, the Early Mesozoic granitoids (243–192 Ma) are predominantly disseminated (Fig. 1b; Zhang et al., 2005, 2015). The granitoids include varieties of monzogranite and I-type granodiorite portraying geochemical attributes analogous to the bulk continental crust. During continental collision stages, these rocks are generated because of melting of amphibolite of MORB protolith (Zhang et al., 2015). In particular, the western Kunlun orogenic belt is a renowned place due to the presence of high-quality gemstone nephrite (Liu et al., 2016) and the belt is deliberated as vital and gigantic Cu–Pb–Zn–Au bearing deposit which makes western Kunlun an important metallogenic belt both in China and Central Asia (Sun et al., 2003; Z.W. Zhang et al., 2014). Four classes of abundant ore deposits have been documented in the belt (Fig. 1b). These comprise (1) Cu bearing sandstone (Sun et al., 2003), (2) Cu–Mo–Fe magmatic hydrothermal deposits (Liu et al., 2010), (3) Cu-Zn volcanic massive sulfide deposits (Sun et al., 2003), and (4) Cu–Pb–Zn-Au–Co carbonate deposits (Z.W. Zhang et al., 2014). The Cu bearing sandstone is present in the Early Carboniferous red terrigenous bodies (Sun et al., 2003), however, magmatic-hydrothermal Cu–Mo–Fe deposits are thoroughly linked with certain felsic intrusions. According to Liu et al. (2010), the zircon U-Pb age of ore-bearing granitoids is 251 ± 5 Ma. In addition, the Cu–Pb–Zn carbonate deposits are identified in two episodes of mineralization (337–331 and 235–206 Ma; Z.W. Zhang et al., 2014). On the contrary, volcanic massive sulfide deposits are introduced in the Carboniferous volcanic rocks signifying Rb-Sr isochron age of 332 ± 66 Ma (Sun et al., 2003). Thus, the presented geochemical data propose that the four kinds of deposits mentioned above were developed in the Late Paleozoic time. However, the research work on Ordovician granitoid was undecided, though such granitoids broadly dispersed in the area. Leng et al. (2018) explored these granites comprehensively based on isotopic composition and implied that such rocks are possibly source of tungsten and could be responsible for commercial Mo–W–Cu mineralization, formed at the episode of 450 Ma in western Kunlun.

3. Deposit geology

The low-grade metamorphosed terrigenous bodies, marble, metavolcanics and subordinate garnet bearing skarns are the main outcrops of Kukaazi and these are collectively named as Middle Proterozoic Changcheng Assemblage. Additionally, the exposed Ordovician granitoids possess chiefly granodiorite, monzonite and subsidiary alkali

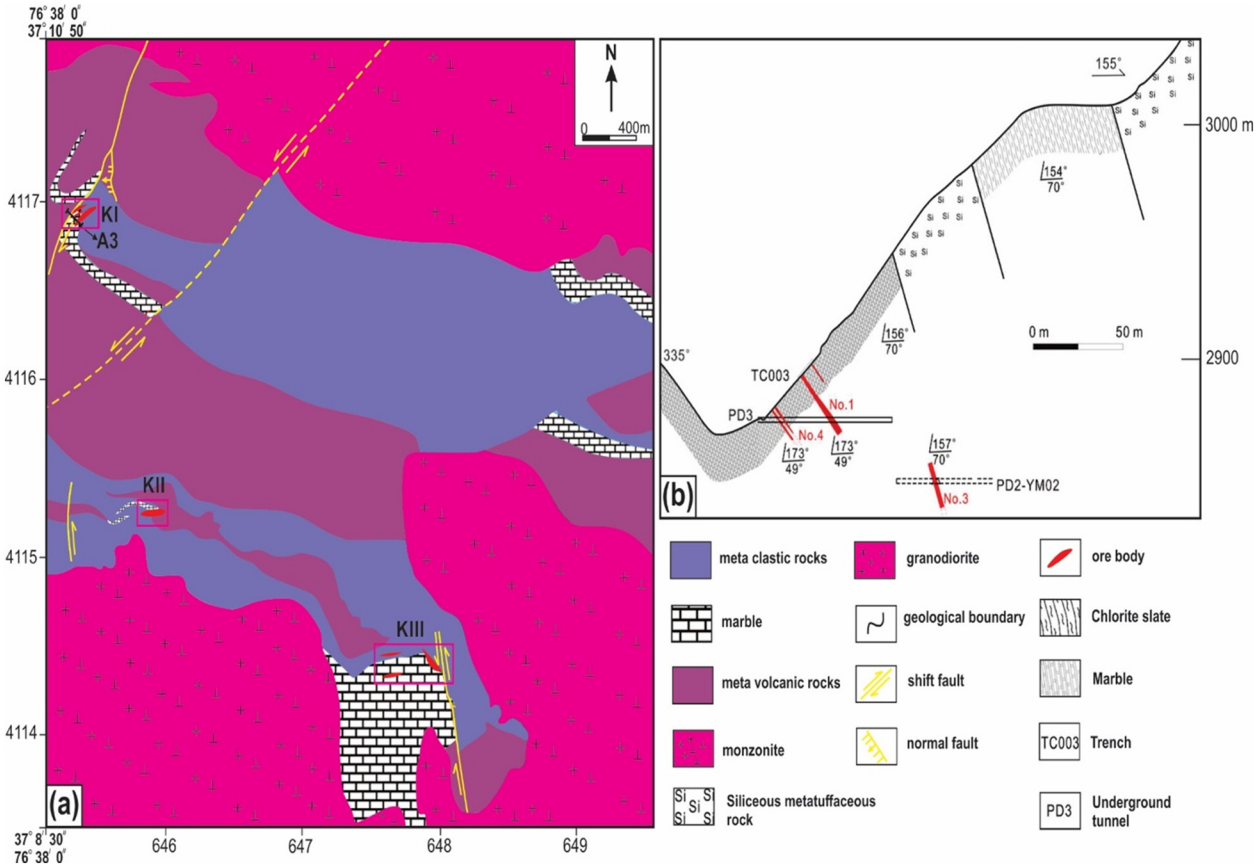

Fig. 2. a, b Geological map of Kukaazi deposit and its cross section along line A3 (modified after Leng et al., 2018).

granite. These plutons subsequently intruded the metamorphosed bodies during span of 462–456 Ma (Y.H. Wang et al., 2013). Geochemical attributes of the granitoids reveal metaluminous I-type character and compositional nature having 0.91–1.05 A/CNK values. Meanwhile, the plutonic bodies are interpreted to be deficient in high field strength elements, comparatively augmented in light rare earth and large ion lithophile elements and signify negative $\varepsilon_{Hf}(t)$ values along with high Sr isotopic ratios (Yuan et al., 2003; C. Wang et al., 2013; Jia, 2013). Therefore, these were suggested to be produced from partial melting of the mafic lower crust in tectonic settings of active continental arc (Yuan et al., 2003; C. Wang et al., 2013; Y.H. Wang et al., 2013).

The Mesoproterozoic Changcheng Group comprises outcrops of meta-volcanics, marble, mica quartz and chlorite slate. Ore bodies mostly recognized in lenses and vein form in these low-grade metamorphic varieties. Three ore blocks namely KI, KII, and KIII have been delineated in the mine in accordance with mineral grouping and spatial distribution (Fig. 2a; Leng et al., 2018). Mineralogically, the KI ore block contains varieties of major ore minerals including scheelite, chalcopyrite, galena and sphalerite. However, arsenopyrite, molybdenite, bismuthinite, pyrrhotite, pyrite and tetrahedrite are perceived as subordinate minerals in northwestern part of mine. Besides, the garnet skarn ore contains sulfides, garnet, scheelite, marble and quartz. Minerals exist in the form of veins and patches in this ore body. The ores are chiefly present in garnet skarns layers between a footwall which represents presence of siliceous meta-tuffaceous rocks and a hanging wall, characterized by laminated marble (Fig. 2b). The marble ore is specified by occurrence and abundance of sulfide minerals including pyrite, galena, sphalerite and arsenopyrite which are extensively dispersed in the Changcheng Group (Fig. 2b). More importantly, a gigantic Cu–W–(Zn-Pb) bearing ore body is observed. The gangue minerals in this body occur as carbonates, garnet, quartz and subordinate fluorite however, economically it comprises 0.2–0.92 wt% W, 0.9 wt% Cu, 0.3 wt% Pb and 0.8 wt% Zn. In contrast, the KII ore block situated at the middle of mine is marked by presence of crystalline marble and tuffaceous slate. These ore bodies are recognized as lenticular containing mineralogically sulfides varieties particularly chalcopyrite, galena, sphalerite, pyrite, pyrrhotite along with magnetite and the average ore grades are determined as Zn 9.9 wt% and Pb 13.7 wt%. Conversely, the KIII ore block of garnet-diopside skarns located at the southeastern part of mine is mainly in the form of lenses comprising assemblage of metallic minerals including sphalerite, arsenopyrite, galena, pyrite and magnetite.

X.C. Zhang et al. (2014) demonstrated paragenesis of two phases of mineralization in the Kukaazi deposit involving early diagenesis and late magmatic-hydrothermal. The diagenetic process was delineated in massive sulfide ores of marble comprising pyrite, sphalerite, galena and pyrrhotite however, the linkage of scheelite, sphalerite, galena, molybdenite, chalcopyrite, pyrrhotite and arsenopyrite in veinlets implies that they were developed through activity of magmatic-hydrothermal fluids.

4. Analytical methods

We systematically collected fresh specimens of granites from the outcrops of the Kukaazi deposit. The granite is massive and shows porphyritic texture with presence of some microcline phenocrysts (Fig. 3a). The rock samples were deprived of noticeable alteration. All the apatite grains under analysis were separated using conventional heavy liquid and magnetic separation techniques, and then were handpicked under binocular microscope. Some euhedral apatite grains (ca. 150 grains per sample) without other inclusions were selected to be mounted in epoxy mounts which were then polished to section the crystals in half for observation and analysis. All analyzed apatite grains

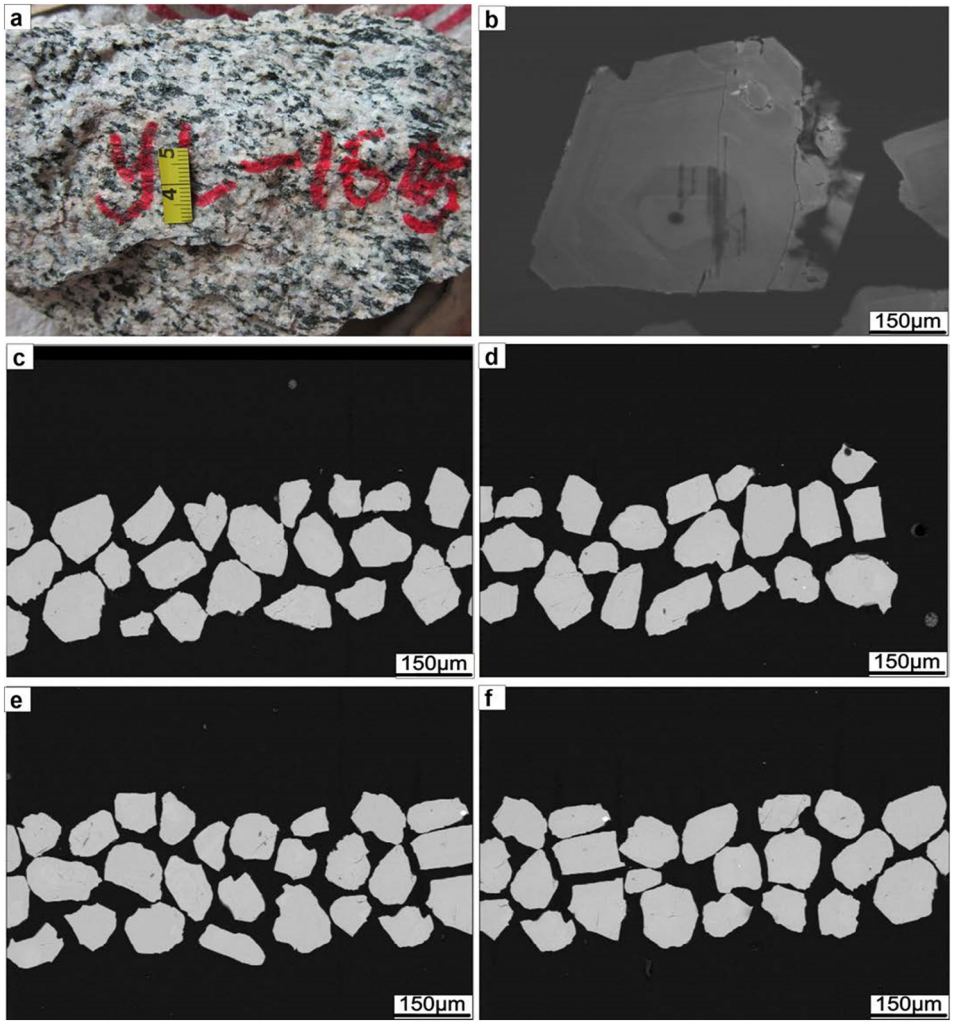

Fig. 3. a reveals coarse grained Kukaazi granite, and b-f Presence of primary crystallized apatite crystals from Kukaazi pluton.

were documented under optical microscope and scanning electron microscopy (SEM) to reveal their external and internal structures. Cathode luminescence (CL) images were collected on an FEI Quanta 600 environmental scanning electron microscope (Central Science Laboratory, University of Tasmania) equipped with a Gatan Pana CLF CL detector. Imaging was carried out on polished and carbon coated samples at an accelerating voltage of 20 kV and beam current of around 3 nA.

Chemical compositions of apatite were analyzed using an EPMA-1600 electron probe at the State Key Laboratory of Ore Deposit Geochemistry, Institute of Geochemistry Chinese Academy of Sciences. The wavelength dispersive technique was employed in this study. Standard operating conditions include 25 kV for accelerating voltage, 10 nA for specimen current, and 10 μm for beam diameter. SPI mineral standards (USA) were used for calibration. Other analysis was completed at the Central Science Laboratory, University of Tasmania using a SX-100 CAMECA EMPA. Analyses of apatite were performed at 15 kV and 10 nA using a defocused 10 μm diameter beam. The analytical results for the same spot obtained from these two laboratories agree well. In-situ trace element analysis of apatites were performed using a Wave UP-213 Laser Ablation System coupled with an Agilent 4500 ICP-MS quadrupole inductively coupled plasma-mass spectrometer (LA-ICP-MS) at the CODES, University of Tasmania. The analytical protocol employed is similar to that outlined in Bonyadi et al. (2011). In this course, the content (wt%) of CaO determined by EMPA was employed as internal calibration. The NIST SRM 612 glass was used as a primary standard to monitor instrumental drift and mass bias, and the GSD-1g glass was taken as secondary standard reference for calculating element concentrations. The accuracy of the laser ablation protocol employed here was assessed by repeat analysis of the matrix-matched, in-house Durango apatite standard.

During the analytical process, the NIST SRM 612 standard was ablated using a 80 μm spot size, 10 Hz repetition rate, and 80% power output corresponding to an energy density of 3.48 J/cm^2, while the GSD-1g glass, Durango Apatite, and our apatite grains were ablated using a 32 μm spot size. Analysis was conducted in a He atmosphere (0.7 to 1.0 l/min) within the ablation cell, and mixed with Ar (0.6 to 1.0 l/min) prior to entering the torch assembly. A typical analysis consisted of a ~30 s background measurement followed by data acquisition and ablation for ~60 s using a rapid peak jumping and dwell time of 28 ms for each element reported. Data reduction, including concentration determinations, method detection limits and internal uncertainties were obtained using SILLS 1.2 software. After inspection of the spectra, signal intervals for integration were selected in order to avoid those regions which were obviously contaminated or represented signals from small cracks or the glass mount.

5. Results

5.1. Major elements

The elemental compositions of apatite from the Kukaazi deposit are given in Tables 1 and 2. It contains 0.01–0.21 wt% Na_2O (average

Table 1
Major and minor elements concentrations (wt%) of the apatite from Kukaazi granite samples.

Sample	F	P_2O_5	CaO	Cl	MnO	FeO	SO_3	Na_2O	SiO_2	MgO	Al_2O_3	K_2O	O = F, Cl	Total
YL-165-1	3.54	42.24	54.84	0.07	0.04	0.02	0.03	0.01	0.40	–	–	–	1.50	99.68
YL-165-2	3.90	42.71	55.39	0.05	0.05	b.d.	0.03	b.d.	0.18	–	–	–	1.65	100.66
YL-165-3	4.25	42.88	55.59	0.04	0.05	0.01	0.02	0.04	0.05	–	–	–	1.80	101.14
YL-165-4	3.66	42.76	54.76	0.05	0.07	0.03	0.04	0.04	0.19	–	–	–	1.55	100.03
YL165-4-1[C]	3.63	42.32	54.74	0.03	0.06	0.04	0.05	b.d.	0.03	b.d.	b.d.	b.d.	1.54	99.37
YL165-4-2[C]	3.51	42.21	54.30	0.06	0.09	0.02	0.03	0.01	0.13	b.d.	0.01	b.d.	1.49	98.87
YL165-4-3[C]	3.46	41.57	54.29	0.04	0.05	0.03	0.01	b.d.	0.36	0.01	b.d.	b.d.	1.47	98.35
YL-165-5	3.58	41.46	55.73	0.07	0.06	0.02	0.02	b.d.	0.33	–	–	–	1.52	99.74
YL-165-6	4.18	42.03	56.00	0.04	0.06	0.03	0.07	0.02	0.08	–	–	–	1.77	100.75
YL-165-7	3.81	41.39	55.49	0.05	0.06	0.01	0.08	0.04	0.32	–	–	–	1.61	99.63
YL-165-8	4.23	41.90	55.37	0.05	0.06	0.04	0.09	0.05	0.13	–	–	–	1.79	100.11
YL-165-9	3.76	42.64	56.63	0.03	0.03	0.01	0.05	0.02	0.14	–	–	–	1.59	101.70
YL-165-10	4.13	41.85	55.17	0.05	0.08	0.04	0.02	b.d.	0.31	–	–	–	1.75	99.90
YL165-10-1[C]	3.84	42.51	54.91	0.03	0.08	0.02	0.06	b.d.	0.04	b.d.	b.d.	0.01	1.62	99.87
YL165-10-2[C]	3.60	41.87	54.41	0.06	0.06	0.01	b.d.	b.d.	0.39	b.d.	b.d.	0.01	1.53	98.90
YL165-10-3[C]	3.57	41.67	54.19	0.06	0.04	0.02	0.03	b.d.	0.66	b.d.	b.d.	b.d.	1.52	98.71
YL-165-11	4.02	42.01	55.78	0.04	0.07	0.02	0.08	0.05	0.29	–	–	–	1.70	100.67
YL-165-12	3.74	41.70	55.60	0.06	0.06	b.d.	b.d.	0.03	0.38	–	–	–	1.59	99.99
YL-165-13	3.68	41.00	55.33	0.06	0.06	0.06	0.02	0.03	0.44	–	–	–	1.56	99.12
YL-165-14	3.68	41.59	56.20	0.06	0.08	0.01	0.05	0.03	0.28	–	–	–	1.56	100.39
YL-165-15	3.96	42.25	55.71	0.05	0.05	0.03	0.12	0.04	0.09	–	–	–	1.68	100.62
YL-YT-1-1	3.38	42.49	55.08	0.06	0.04	0.02	0.02	0.03	0.13	–	–	–	1.44	99.81
YL-YT-1-2	3.45	42.90	55.01	0.09	0.04	0.02	b.d.	0.07	0.16	–	–	–	1.47	100.26
YL-YT-1-3	3.49	42.48	54.94	0.07	0.08	0.01	0.01	0.01	0.25	–	–	–	1.49	99.86
YL-YT-1-4	3.60	42.63	54.89	0.07	0.09	b.d.	0.01	0.02	0.18	–	–	–	1.53	99.95
YL-YT-1-5	3.58	43.19	55.78	0.06	0.06	0.02	0.02	b.d.	0.14	–	–	–	1.52	101.33
YL-YT-1-6	3.39	42.53	55.55	0.06	0.07	0.02	b.d.	0.03	0.18	–	–	–	1.44	100.38
YL-YT-1-7	3.66	42.84	54.96	0.05	0.08	0.02	0.01	0.04	0.21	–	–	–	1.55	100.32
YL-YT-1-8	3.59	42.79	55.45	0.04	0.05	0.02	0.01	0.01	0.21	–	–	–	1.52	100.64
YL-YT-1-9	3.38	43.28	55.71	0.05	0.07	0.01	0.03	0.02	0.02	–	–	–	1.43	101.14
YL-YT-1-10	3.47	42.05	55.25	0.07	0.09	0.02	0.01	0.01	0.34	–	–	–	1.48	99.83
YL-YT-1-11	3.48	42.99	54.86	0.08	0.06	0.02	0.02	0.03	0.15	–	–	–	1.48	100.21
YL-YT-1-11[C]	3.39	42.74	55.00	0.06	0.06	0.03	b.d.	0.01	0.17	b.d.	b.d.	b.d.	1.44	100.02
YL-YT-1-12	3.42	42.17	55.46	0.06	0.07	0.01	0.04	b.d.	0.36	–	–	–	1.45	100.12
YL-YT-1-12[C]	3.41	41.47	54.20	0.06	0.06	0.01	0.01	b.d.	0.48	0.01	b.d.	b.d.	1.45	98.26
YL-YT-1-13	3.36	42.64	54.65	0.07	0.05	0.02	0.02	0.01	0.11				1.43	99.51
YL-YT-1-13-1[C]	3.45	42.09	54.82	0.07	0.06	0.01	b.d.	0.04	0.22	b.d.	b.d.	0.02	1.47	99.30
YL-YT-1-13-2[C]	3.34	42.34	54.73	0.07	0.08	0.01	b.d.	0.01	0.13	b.d.	b.d.	0.02	1.42	99.30
YL-YT-1-13-3[C]	3.52	42.16	55.00	0.08	0.03	b.d.	0.02	0.06	0.11	b.d.	0.01	b.d.	1.50	99.51
YL-YT-1-14	4.43	42.74	55.37	0.15	0.05	0.02	0.02	b.d.	0.21	–	–	–	1.90	101.09
YL-YT-1-15	3.45	41.66	54.09	0.06	0.05	b.d.	b.d.	b.d.	0.53	–	–	–	1.47	98.37
YL-YT-1-15-1[C]	3.38	42.22	54.68	0.07	0.07	b.d.	b.d.	b.d.	0.24	b.d.	b.d.	b.d.	1.44	99.22
YL-YT-1-15-2[C]	3.38	42.20	54.45	0.05	0.06	0.02	0.01	b.d.	0.26	b.d.	b.d.	b.d.	1.44	99.00
YL-YT-1-15-3[C]	3.42	42.73	54.35	0.07	0.11	0.01	0.01	b.d.	0.23	b.d.	b.d.	b.d.	1.46	99.48
YL-YT-2-1	3.63	42.10	54.73	0.04	0.04	0.01	0.14	0.02	0.38	–	–	–	1.54	99.56
YL-YT-2-2	3.80	42.63	55.75	0.09	0.05	0.01	0.15	0.05	0.16	–	–	–	1.62	101.05
YL-YT-2-2-1[C]	3.41	41.93	54.43	0.07	0.06	0.04	0.16	0.01	0.36	0.01	b.d.	0.01	1.45	99.03
YL-YT-2-2-2[C]	3.51	42.65	54.85	0.07	0.06	0.02	0.15	0.02	0.14	0.01	0.03	b.d.	1.49	100.01
YL-YT-2-2-3[C]	3.51	41.75	54.68	0.06	0.09	0.05	0.10	0.05	0.24	0.01	0.02	b.d.	1.49	99.07
YL-YT-2-3	3.57	42.20	55.20	0.07	b.d.	0.03	0.21	0.03	0.26	–	–	–	1.52	100.05
YL-YT-2-3-1[C]	3.29	40.98	54.28	0.07	0.05	0.01	0.63	0.21	0.43	b.d.	b.d.	b.d.	1.40	98.55
YL-YT-2-3-2[C]	3.13	42.10	54.43	0.11	0.03	0.02	0.14	0.03	0.34	b.d.	b.d.	b.d.	1.34	99.00
YL-YT-2-3-3[C]	3.51	41.68	54.89	0.05	0.04	0.02	0.17	0.02	0.22	b.d.	b.d.	b.d.	1.49	99.12
YL-YT-2-4	3.33	42.70	54.98	0.06	0.03	0.03	0.17	0.01	0.25	–	–	–	1.42	100.15
YL-YT-2-5	3.68	42.66	55.33	0.07	0.06	0.01	0.16	0.04	0.21	–	–	–	1.57	100.65
YL-YT-2-6	3.61	42.93	55.36	0.05	0.07	0.02	0.16	0.11	0.21	–	–	–	1.53	100.98
YL-YT-2-7	3.43	41.97	54.43	0.07	0.01	0.02	0.20	0.04	0.35	–	–	–	1.46	99.05
YL-YT-2-8	3.55	42.54	55.11	0.07	0.07	b.d.	0.20	0.05	0.25	–	–	–	1.51	100.33
YL-YT-2-8-1[C]	3.13	41.99	54.52	0.07	0.03	b.d.	0.17	b.d.	0.22	b.d.	0.01	b.d.	1.33	98.82
YL-YT-2-8-2[C]	3.47	42.36	55.10	0.05	0.04	0.01	0.17	0.07	0.13	0.02	0.01	b.d.	1.48	99.95
YL-YT-2-9	3.35	42.10	54.59	0.04	0.03	b.d.	0.15	0.02	0.26	–	–	–	1.42	99.12
YL-YT-2-10	3.43	42.12	55.29	0.08	0.04	b.d.	0.17	0.02	0.33	–	–	–	1.46	100.03
YL-YT-2-11	3.78	42.67	55.75	0.06	0.05	0.01	0.13	0.04	0.16	–	–	–	1.60	101.03
YL-YT-2-12	3.32	42.73	55.90	0.08	0.05	0.01	0.13	0.03	0.17	–	–	–	1.42	101.02
YL-YT-2-13	3.72	42.51	54.84	0.07	0.03	0.02	0.16	0.05	0.35	–	–	–	1.58	100.16
YL-YT-2-14	3.47	42.74	54.76	0.09	0.05	0.02	0.15	0.03	0.28	–	–	–	1.48	100.11
YL-YT-2-15	4.00	42.09	54.66	0.08	0.04	b.d.	0.14	0.02	0.44	–	–	–	1.70	99.76
YL-YT-2-15-1[C]	3.58	42.10	54.57	0.07	0.08	b.d.	0.17	0.03	0.27	b.d.	0.03	b.d.	1.52	99.37
YL-YT-2-15-2[C]	3.74	41.66	54.88	0.06	0.04	b.d.	0.13	b.d.	0.38	b.d.	b.d.	b.d.	1.59	99.30
YL-YT-2-15-3[C]	3.50	41.57	54.71	0.08	0.04	0.03	0.16	0.03	0.36	b.d.	0.06	b.d.	1.49	99.04

Table 2
LA-ICP-MS In-situ trace element compositions (ppm) for apatite from Kukaazi granite samples.

Sample	Na	Mg	Si	Mn	Fe	Sr	Y	La	Ce	Pr	Nd	Sm	Eu	Gd	Tb	Dy	Ho	Er	Tm	Yb	Lu	Pb	Th	U	*Eu
YL-165-1	17.2	27.2	2222	469	184	167	2222	925	3147	470	2203	506	41.2	489	63.6	374	73.4	210	28.5	189	27.8	22.7	167	85.5	0.25
YL-165-2	26.5	33.0	1663	515	232	173	1370	917	2842	393	1693	324	26.7	281	35.6	209	42.1	127	18.4	127	19.8	18.1	129	66.7	0.26
YL-165-3	88.1	19.2	329	391	146	168	183	59	210	32	156	36.3	6.6	36.6	4.5	27.1	5.7	16.8	2.4	16.3	2.7	5.4	5.4	11.7	0.55
YL-165-4-1	114.5	32.2	b.d.	498	216	174	137	105	288	39	166	33.1	6.6	32.1	3.6	21.1	4.2	12.9	1.8	12.3	2	7	8.1	14	0.61
YL-165-4-3	19.3	36.5	1527	531	252	172	1227	951	2794	372	1560	295	30.4	260	32	186	38	116	16.3	115	18.3	25.7	82.8	93.6	0.33
YL-165-6	98.4	42.5	474	518	226	173	302	138	409	58	262	58.2	11.3	59.5	7.5	45.3	9.5	28.1	3.8	28.5	5	9.9	22.1	29.1	0.58
YL-165-7	b.d.	27.1	2080	467	176	169	1568	982	3166	450	2010	403	37.3	366	44.9	257	50.6	147	20.4	141	22	16	116	54.9	0.29
YL-165-8	73.4	28.8	863	454	190	170	517	249	740	107	503	114	19.2	117	14.5	83.5	16.9	48.5	6.4	42.9	6.9	16.4	39.1	57.8	0.5
YL-165-9	18.7	22.9	1234	413	172	162	1602	286	1119	196	1052	286	32.3	305	41.3	247	51.1	152	21.2	143	22.6	25.5	83.8	94.2	0.33
YL-165-10-2	34.7	45.1	1519	571	297	167	1348	891	2680	365	1559	304	26.9	273	34.2	200	41.8	128	18.7	130	20.9	25.1	67	91.8	0.28
YL-165-10-3	b.d.	28.0	2177	477	207	174	1786	1008	3032	420	1848	387	55.1	370	46.9	275	56	169	23.7	170	27.9	21.1	136	86.3	0.44
YL-165-11	20.0	30.3	1552	483	232	174	1647	584	1897	287	1389	327	39.2	335	43.1	255	52	156	21.7	149	24	25	b.d.	b.d.	0.36
YL-165-15	132	21.2	833	424	180	165	305	131	407	58	278	62.4	13.4	64	7.9	44.9	9.7	29.6	3.9	29.9	5.4	10.9	19.7	31	0.64
YL-YT-1-1	101	12.7	636	662	156	611	311	592	1505	194	845	142	18.8	122	13.2	70.9	12.4	29.4	3.3	17.9	2.1	6.2	18.9	8.1	0.42
YL-YT-1-2	136	25.6	658	796	164	602	353	704	1690	210	883	144	20.3	125	14.2	72.4	13.4	33.2	3.8	20.4	2.8	6.9	18.5	8.2	0.45
YL-YT-1-4	129	18.8	836	682	132	520	365	528	1430	195	906	169	14	150	16.4	84.1	14.9	35.6	3.7	20.2	2.4	6.7	15.8	7.1	0.26
YL-YT-1-5	61.3	18.7	752	581	161	517	255	438	1142	150	669	116	14.4	101	10.9	56	10.1	24	2.6	13.3	2	5.8	14.4	7.5	0.4
YL-YT-1-6	96.1	22.5	1592	836	150	617	845	1461	3629	459	1966	343	45.5	292	33	177	32.3	80.8	9.1	52.3	6.7	9.7	75.9	22.3	0.43
YL-YT-1-7	62.1	14.8	890	532	278	305	364	430	1263	173	793	138	18.1	125	13.4	72.8	13.5	33.8	4	24.5	3.7	10.8	18.2	18.8	0.41
YL-YT-1-11	47.4	18.5	1030	632	151	466	494	892	2249	282	1191	195	25.1	164	18.8	98.9	18.2	47.5	5.6	33.3	4.4	7.9	42.4	14.8	0.42
YL-YT-1-12	33.3	19.3	2050	634	171	450	1039	1633	4150	529	2278	398	48.6	340	38.4	210	38.5	98	11	64.4	8.3	11.8	95.6	31.1	0.39
YL-YT-1-13-1	67.3	20.5	816	577	149	468	488	815	2158	278	1213	204	23.7	177	19.5	104	18.8	46.7	5.3	29	3.9	7.2	35.2	15	0.37
YL-YT-1-13-2	74.2	17.0	519	607	146	464	266	423	1104	144	641	108	13.2	96.5	10.5	55.6	10.1	26	2.8	15.9	2.3	5.8	14.1	7.1	0.39
YL-YT-1-15-1	24.0	22.0	2049	615	162	413	1080	1671	4320	558	2423	424	48.3	364	41.8	226	41.1	104	12.1	69.6	9.3	11.2	84	31.5	0.37
YL-YT-1-15-2	55.9	18.5	1295	620	143	518	668	1166	2934	372	1606	277	31.2	238	26.9	144	25.8	63.6	7.2	41.1	5.3	7.6	40.2	14.2	0.36
YL-YT-2-1	107	46.5	992	310	191	323	307	498	1377	166	676	105	14.7	91.9	9.2	49.6	9.6	27	3.5	24	4	13.3	129	45.8	0.45
YL-YT-2-4	168	37.5	928	415	182	352	184	521	1219	131	472	63.6	14.7	49.8	5.2	27.6	5.4	16	2.4	15.9	2.8	8.4	67.3	20.7	0.77
YL-YT-2-6	66.6	11.9	1038	328	116	331	306	408	1153	141	579	92.1	16.9	81.4	8.8	47.1	9.4	27.4	3.8	27.6	4.9	20.5	158	75.8	0.58
YL-YT-2-7	188	21.1	1468	449	174	397	229	1504	2756	253	832	101	17.9	77.8	7.7	38.9	7.3	20.5	2.7	18.3	2.8	10.5	126	28.9	0.59
YL-YT-2-8-1	102	15.9	1420	377	126	335	228	755	1738	183	658	86.6	17	67.5	6.9	35.8	6.8	19.7	2.7	18.3	3.2	9.7	96	30.3	0.65
YL-YT-2-8-2	112	18.1	568	365	149	330	97	226	528	58	221	32.7	7.3	27.5	2.8	14.7	3	8.5	1.1	8.2	1.5	11.7	25.3	42.4	0.72
YL-YT-2-9	115	12.4	1241	353	116	324	311	739	1695	186	714	105	21.1	86.3	9.1	48.1	9.5	27.9	3.8	26.7	4.6	11.7	95.9	36.1	0.66
YL-YT-2-10	113	16.1	1464	381	129	341	402	863	2105	233	872	129	26.5	108	11.4	62.2	12.3	36	5.1	36.3	6.5	28.7	230	108	0.67
YL-YT-2-13	249	11.9	1127	386	113	387	178	1100	2122	205	700	87.6	13.6	65.4	6.5	32.4	6.1	15.7	2	12.5	1.9	6.8	79.1	17.5	0.53
YL-YT-2-14	193	30	1177	483	198	398	189	1027	2077	202	686	84	14.8	63.4	6.5	33.2	5.9	17.1	2.2	14.8	2.2	9.2	91.7	22.1	0.6
YL-YT-2-15-1	131	14.2	1010	371	149	341	231	553	1438	164	629	91.6	17.5	70.3	7.4	38.8	7.3	21.3	2.8	19.7	3.4	11.5	87.9	35.4	0.64
YL-YT-2-15-2	80.3	14.2	1841	375	120	335	418	1262	3175	347	1288	175	32.3	136	13.9	72.6	13.6	38.3	5.1	35.2	5.8	17.6	202	60.3	0.62
YL-YT-2-2-1	183	16	745	433	147	361	144	575	1274	132	477	65.5	11.3	48.6	4.9	25.7	4.8	12.9	1.7	10.8	1.8	6.5	40.8	14.4	0.59
YL-YT-2-2-3	168	15.5	1149	412	127	351	300	833	1890	204	750	108	22.1	85.7	9.4	49.5	9.5	27.2	3.7	25.2	4.4	11	98.5	34.2	0.68
YL-YT-2-3-1	338	27.5	1741	497	206	410	253	1406	2795	274	925	115	19.3	86.8	8.9	45.2	8.4	22.9	2.9	19.2	2.9	10	110	25.3	0.57
YL-YT-2-3-3	87.4	13.6	885	344	123	329	163	446	942	101	399	58	12.1	50.3	5.1	26.3	5.2	14.6	1.9	13.5	2.4	12.9	64	42.3	0.67

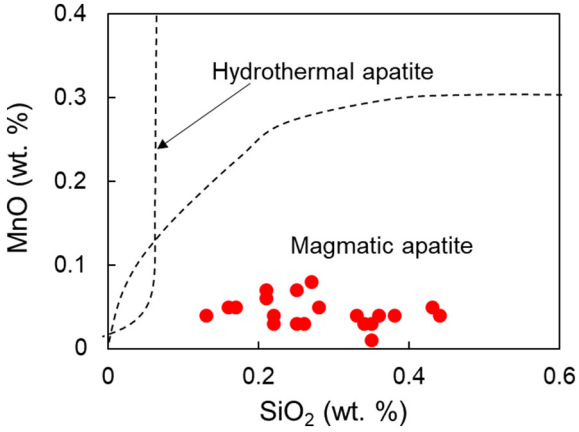

Fig. 4. Plot of SiO_2 (wt%) vs. MnO (wt%) for apatite hosted in Kukaazi granite (fields from Chen et al., 2017).

0.03 wt%), 0.01–0.11 wt% MnO (average 0.05 wt%), 0.01–0.06 wt% FeO (average 0.02 wt%), 40.98–43.28 wt% P_2O_5 (average 42.24 wt%), 54.09–56.63 wt% CaO (average 55.04 wt%), 0.01–0.63 wt% SO_3 (average 0.10 wt%), 3.13–4.43 wt% F (average 3.59 wt%), 0.03–0.15 wt% Cl (average 0.06 wt%) and 0.02–0.66 wt% SiO_2 (average 0.25 wt%). Cl/F ratio is in the range of 0.007–0.03, average 0.01. The contents of K_2O, MgO and Al_2O_3 are very low, observed as below the detection limit. All the studied grains of apatite reveal higher contents of fluorine. Hence, the apatites of the Kukaazi deposit can be classified as fluorapatite. In the SiO_2-MnO diagram, all the examined apatites plot in the field of magmatic apatite (Fig. 4), signifying that the apatites composition reflects the parental magma characteristics.

The results show that the contents of MnO, SiO_2 and FeO are low in apatite samples; however concentrations of P_2O_5 and CaO are very higher, considered as the essential components of apatite. In addition, the contents of Na_2O and SO_3 in the apatite crystals are very low however, some of the samples are also perceived as below the detection limit. The positive correlation of these two oxides possibly depicts the coupled substitution in apatites (Sha and Chappell, 1999); nevertheless, the results of present study do not show any absolute correlation between Na_2O and SO_3 (Fig. 5a). Furthermore, plotting between F and Cl concentrations indicate negative correlation in apatite (Fig. 5b). The results also indicate that all the samples of apatite are enriched in F (3.13–4.43 wt%, average 3.59 wt%) but poor in Cl (0.03–0.15 wt%, average 0.06 wt%).

5.2. Trace elements

The Y, Sr and Mn contents of apatite from the Kukaazi granites are in the ranges of 97.2–2222.1 ppm (average 627.85 ppm), 161.5–617.2 ppm (average 339.11 ppm) and 310.2–836.1 ppm (average 497.87 ppm), respectively. The distribution of Sr and Y plotting do not reveal any clear correlation (Fig. 6a) whereas, Sr and Mn plotting indicate positive correlation (Fig. 6b). Moreover, the concentrations of Pb, Th and U in apatite are 5.4–28.7 ppm (average 13.03 ppm), 5.4–229.7 ppm (average 78.22 ppm) and 7.1–108.3 ppm (average 39.46 ppm) respectively. The Th and U as well as the apatite Th/U ratio and Sr plot exhibits positive correlation (Fig. 6c, d). The results of high Th/U ratio (4.52) and low Th/U ratio (0.46) are possibly attributable to low abundance and greater contents of uranium respectively. Meanwhile, the concentrations of La, Ce, Pr, Nd and Sm exhibit larger variation in the range of 58.6–1671.1 ppm (average 754.03 ppm), 209.5–4319.8 ppm (average 1932.89 ppm), 32.4–557.9 ppm (average 240.91 ppm), 155.5–2423.3 ppm (average 1012.76 ppm) and 32.7–506.3 ppm (average 182.17 ppm), respectively. In contrast, the contents of Eu, Gd, Tb, Dy, Ho, Er, Tm, Yb and Lu vary from 6.6 to 55.1 ppm (average 23.44 ppm), 27.5–488.5 ppm (average 162.63 ppm), 2.8–63.6 ppm (average 19.22 ppm), 14.7–374.4 ppm, (average 107.73 ppm), 3–73.4 ppm (average 20.94 ppm), 8.5–209.6 ppm (average 58.94 ppm), 1.1–28.5 ppm (average 7.78 ppm), 8.2–188.9 ppm (average 51.57 ppm) and 1.5–27.9 ppm (average 7.97 ppm), respectively. In addition, the δCe and the δEu values are (0.98–1.15, average 1.08) and (0.25–0.77, average 0.49) respectively. Apart from these, the apatite display (La/Yb) N value 1.35–59.33, average 18.48 and (La/Sm) N values in the range of 0.63–9.35, average 3.36. The chondrite–normalized rare earth element (REE) diagram exhibits right inclined REE patterns and noticeably moderate degree of negative Eu anomaly (Fig. 7). Besides, this REE pattern also represents significant discrepancies particularly enrichment of light REEs (LREEs; La-Sm) comparative to heavy REEs (HREEs; Eu-Lu) in apatite (Fig. 7).

6. Discussion

6.1. Geochemical attributes of REEs and Sr in magmatic apatite of the Kukaazi granite

The analytical interpretation of Eu particularly its negative Eu anomaly (Drake, 1975), indicates that the plagioclase crystallization reduces Eu in magma, triggering and causing small concentration of europium in apatite. Hence, the distinguishable moderate negative anomaly of europium in the Kukaazi apatite is possibly resulting from plagioclase crystallization earlier than apatite. This observation is

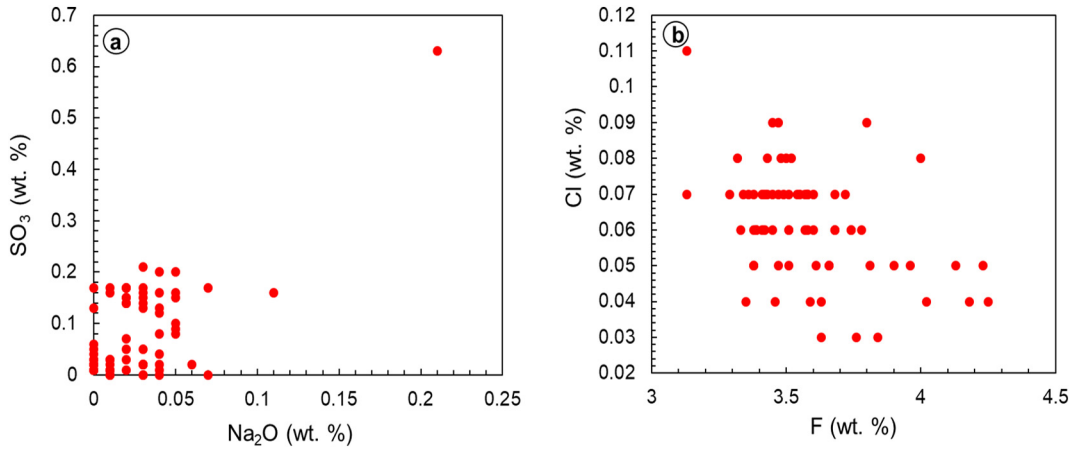

Fig. 5. Plot of (a) apatite SO_3 (wt%) vs. Na_2O (wt%); (b) apatite-F (wt%) vs. Cl (wt%).

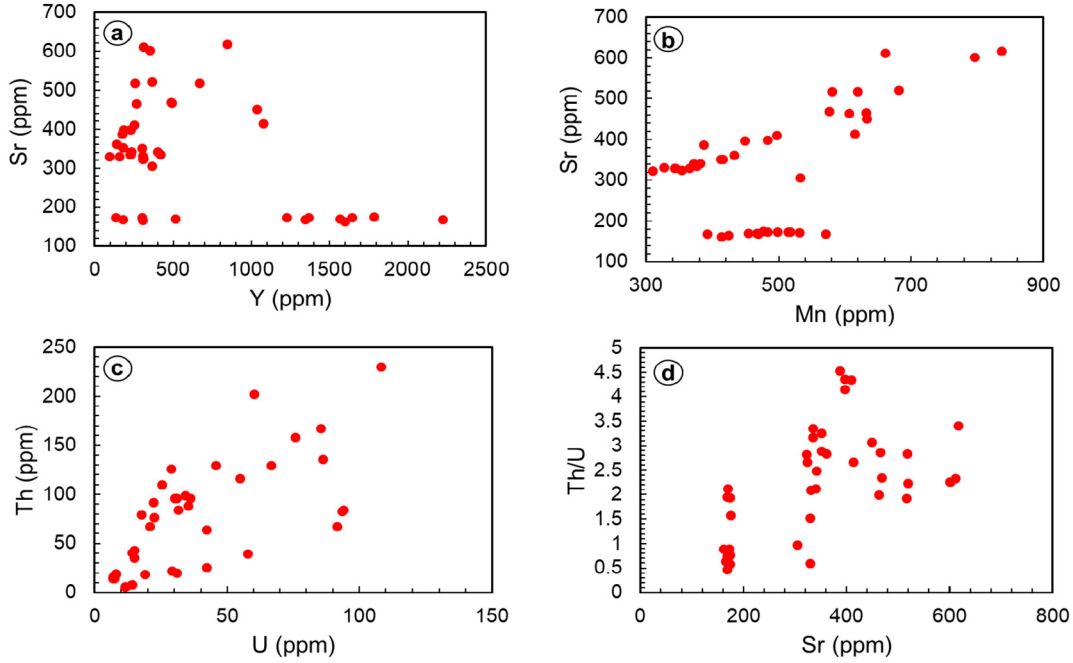

Fig. 6. Plots of (a) Sr (ppm) vs. Y (ppm); (b) Sr (ppm) vs. Mn (ppm); (c) Th (ppm) vs. U (ppm); (d) Th/U vs. Sr (ppm).

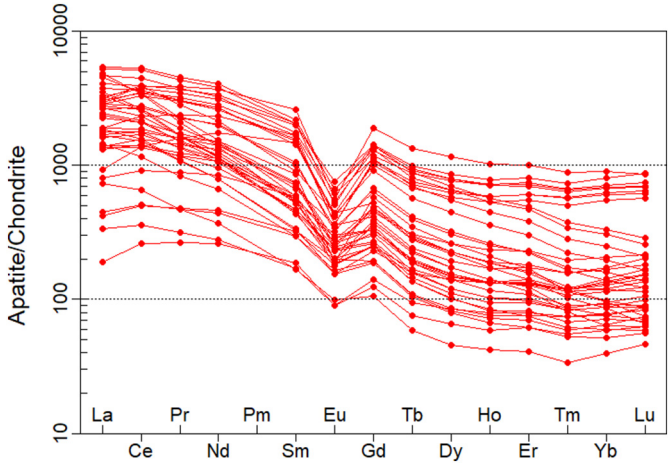

Fig. 7. Chondrite-normalized rare earth element diagram for apatite of Kukaazi deposit (Boynton, 1984).

consistent with the findings of Chen and Zhang (2018). Moreover, the apatite CL images reveal obvious apparent oscillatory zoning, suggesting that the grains of apatite have not experienced noticeable alteration (Fig. 3b). Apatite in CL images frequently shows well-developed crystals demonstrating its crystallization at the early stage (Fig. 3b–f). Hence, the noticed contents of major and trace elements in apatite were primarily governed by their amounts in parental melt and partitioning between apatite/melt. Previous researches propose that the partitioning coefficients of apatite/melt for middle rare earth elements are greater comparative to LREE as well as HREE (Watson and Green, 1981; Fujimaki, 1986), which induces lower values of (La/Sm) N in apatite comparison to the melt. In the current research, the apatite (La/Sm) N values of Kukaazi are in the range of 0.63–9.35 (average 3.36) which are measured as lower than the Kukaazi granites (4.14–9.39, average 7.71, the calculated data for granites are from C. Wang et al., 2013). Therefore, we suggest that higher partitioning coefficients of apatite/melt for middle rare earth elements in comparison to light and heavy REE caused lower values of (La/Sm) N in apatite than granites.

The apatite indicates enrichment of LREE comparative to HREE and exhibits fairly a right inclined distribution pattern (Fig. 7). Zircon is documented to concentrate rare earth elements especially HREEs (Fujimaki, 1986; Klein et al., 1997). According to Chen and Zhang (2018), the saturation temperatures of zircon and apatite are comparable and apatite crystallization is prior than zircon to some extent. Therefore, crystallization of zircon may reveal influence on the composition of apatite, which can cause no clear variances between light and heavy rare earth elements. However, in the current research, presence of zircon has been evaluated and furthermore, obvious differences between light and rare earth elements has been documented. Thus, we propose that the presence of zircon has no impact on apatite composition and resulted in obvious differences between light and heavy REEs. However, further study is required regarding other aspects which may have not affected the apatite composition and generated noticeable distinction between REEs.

In addition, the Sr concentration in apatite grains (161.5–617.2 ppm, average 339.11 ppm) is greater comparative to that of whole-rock (109–603 ppm, average 337 ppm; data from Y.H. Wang et al., 2013). Nevertheless, Chu et al. (2009) proposed that apatite normally comprises less Sr in comparison to host-rock. Therefore, the variation in Sr concentration in Kukaazi apatite is not totally governed by magma composition. Chu et al. (2009) demonstrated that the Sr concentration in apatite is associated to the degree of differentiation and signifies heterogeneity in the magma source. Likewise, Belousova et al. (2001) also proposed that the Sr concentration in apatite reveal variation with the whole-rock. Therefore, the higher Sr content in apatite of Kukaazi deposit can be attributed to restricted crystallization of feldspar (since feldspars favorably concentrate strontium) (Aigner–Torres et al., 2007) or can be ascribed to magmatic involvement from lower crustal or mantle source (Sha and Chappell, 1999; Chu et al., 2009).

6.2. Geochemical characteristics of the magma

The magma oxidation nature can be characterized and evaluated by presence of specific elements in apatite including Eu, Mn, Ce and S (Pan et al., 2016). Furthermore, Ca^{2+} in the apatite can be replaced by Ce^{3+}, Mn^{2+} and Eu^{3+}, thus these elements are easily accommodated into apatite framework (Cao et al., 2012). Ce^{3+}, Mn^{2+} and Eu^{2+} can be

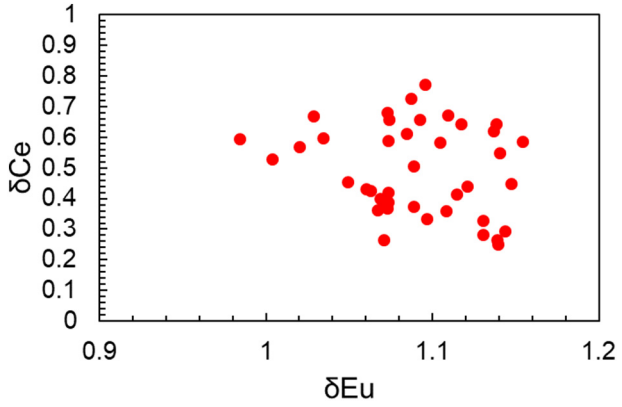

Fig. 8. Plot of δEu vs. δCe for apatite hosted in Kukaazi granite.

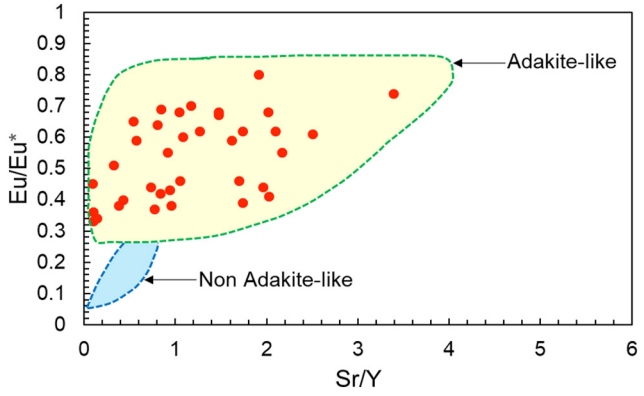

Fig. 9. Plot of Eu/Eu* vs. Sr/Y for apatite of Kukaazi pluton (Fields after Pan et al., 2016).

readily converted to Ce^{4+}, Mn^{4+} and Eu^{3+} under oxidizing state. Higher Ce^{3+}/Ce^{4+}, Eu^{2+}/Eu^{3+} ratios and lower Eu^{3+} concentrations can be produced under low oxygen fugacity conditions, if the physical conditions specifically temperature, likely pressure and composition of bulk rock remain constant (Sha and Chappell, 1999). Therefore, we propose that under the conditions of low oxygen fugacity, the crystallization of Kukaazi apatite generates moderate negative Eu anomaly which is consistent with the findings of Cao et al. (2012). Nevertheless, variations of single element in apatite may not be useful exclusively to evaluate magmatic oxidation condition since it can be influenced by several factors at the time of crystallization of magma. For example, crystallization of plagioclase affects the concentration of Eu in magma and the Eu content may decline as a result of fractionation of plagioclase (Buick et al., 2007; Bi et al., 2002). Thus, in apatite, the multivariance elements having opposite partitioning behavior for instance, Eu and Ce can be effectively significant to evaluate variations in the oxidation state (Pan et al., 2016).

Pan et al. (2016) explored the apatite in granite from the Sanjiang area, exposed in southwestern part of China and deduced that the magma oxidation state can be affected based on negative correlation of δCe and δEu. In the present research, the apatite δCe and δEu values are also interpreted with negative correlation (Fig. 8), suggesting that the variations in values of δEu and δCe are associated to the magma oxidation state. Therefore, the moderate negative Eu anomaly analyzed in the apatite implies that the magmas of Kukaazi granite have moderate oxidizing nature. This finding is similar with the apatite attributes from Cu-Mo and Mo-W deposits, exposed in the area of Central Kazakhstan (Cao et al., 2012). The correlation of Ga contents and values of δEu can be valuable to demonstrate the nature of magma; however, samples of present research do not contain Ga contents.

6.3. Implications for differentiating the adakitic and non-adakitic affinity

The apatite Sr/Y and Eu/Eu* ratios are also significant to evaluate the magma characteristics especially magma nature. Pan et al. (2016) deliberated compositions of apatite to discriminate rocks of adakitic and non-adakitic nature in the Sanjiang area, SW China. On the basis of distinguishing adakitic and non-adakitic affinity in apatite, they proposed that apatite which forms from adakitic nature contains greater Sr/Y and Eu/Eu* ratios comparative to that apatite which develops from non-adakitic rocks. These ratios of apatite may also be important to recognize rocks of adakite nature specifically for those which extremely experience alteration and do not sustain the real Sr/Y ratios. Because apatite is not prone to alteration hence can preserve original Sr/Y ratios in contrast to feldspar which is vulnerable to extreme alteration. Nevertheless, it would be very cautiously to apply this scheme when apatite is not in primary stage. Because when apatite crystallization takes place as a result of evolving magma, then it is subjected to immense fractional crystallization which possibly will not reveal original Sr/Y and Eu/Eu* ratios. These original ratios of parental magma will be reflected when development of apatite will be only in earlier phases (Pan et al., 2016). The apatites in the granites of Kukaazi deposit reveal presence of phenocrysts, apparent oscillatory zoning and are mostly euhedral in crystal shape (Fig. 3b–f). These textural characteristics of apatite suggests that it crystallized at earlier phase, therefore preserves the original Sr/Y and Eu/Eu* ratios which can be significant to evaluate the magma characteristics. The Sr/Y and Eu/Eu* values of the Kukaazi apatite are high, plotting in the adakite rock field (Fig. 9), suggesting that the granite of Kukaazi area is adakitic in character. Our finding implies that these ratios of apatite are significant to discriminate the adakitic nature of the rock from non-adakitic ones. Our interpretation of adakitic affinity is consistent with the adakitic character of Cretaceous and Triassic Xiuwacu as well as Pulang Pluton exposed in the Zhongdian terrane (Pan et al., 2016).

6.4. Apatite Cl/F ratio as a robust proxy to track content of magmatic volatiles and mineralization

Chlorine and fluorine show significant character during process of magmatic evolution through depolymerizing the melt configuration and also play vital role in metal transport and ore deposition in hydrothermal system (Filiberto and Treiman, 2009; Harlov, 2015). Nevertheless, tracing the evolution of these volatiles in magmatic system is very complex. The whole-rock chlorine and fluorine contents cannot not directly indicate primary volatile concentrations in the parental magma. However, these can be evaluated by Cl and F-rich minerals, such as apatite (Bonin, 1988; Zhang et al., 2012). Apatite has the unique capability to track the behavior and content of volatiles in magmatic system (Webster et al., 2009). The contents of chlorine and fluorine in the melt can be evaluated from the concentrations of chlorine and fluorine in apatite (Doherty et al., 2014). It is worth noticing that chlorine and fluorine contents resulting from apatite composition do not vary notably in crystallization interval (Zhang et al., 2012). Therefore, Cl/F ratios of the apatite can be considered as primary pointer and fingerprint to trace the composition and content of magmatic volatiles.

The apatite Cl/F ratios in the Kukaazi granite is in the range of 0.007–0.03 (average 0.01). Our results demonstrate that the apatite crystals comprise low Cl/F ratios. It is broadly recognized that apatite is not susceptible to subsolidus halogen exchange (Candela, 1986). Thus, in the fresh samples of Kukaazi apatite, this Cl/F ratio reflects original value in the parental magma from which they crystallized. Hence, our results deliver indirect confirmation for diverse Cl/F ratios in the parental magma of Kukaazi granite. In addition, we have deduced that Cl/F ratio in the parental magma of Kukaazi pluton is low. Li and Hermann (2015) proposed that the low concentration of Cl in apatite exhibits that

the host magma is depleted in chlorine. The prime reason for this might be source control. The apatite Cl concentrations from Kukaazi granite are most probable associated to melt compositions. Apart from this, chlorine quantities in apatite reveal the primary Cl contents of the initial magma (Boyce et al., 2010), signifying that the amounts of volatiles of apatites from Kukaazi granites preserve the halogen compositions of parental magma. Therefore, the main possible reason for depletion of Cl/F ratio in apatite can be attributed to source (magma composition) of the Kukaazi pluton. In the meantime, apatites from this pluton comprises low quantities of Cl and high F suggesting that the parental magma of Kukaazi granite is depleted in chlorine and indicate association with partial melting of lower crust material. Hence, the parental magma of Kukaazi pluton is produced as a result of partial melting of mafic lower crust in settings of active continental arc (Y.H. Wang et al., 2013), a source with low ratio of Cl/F. Slab-derived fluids commonly containing enrichment of Cl, Cl/F ratio and less F are suggestive that the magmas of granitic rocks are associated with slab dehydration. Therefore, we can propose that slab-derived fluids comprising greater Cl/F ratios (Meng, 2014); did not participate in parental magma of Kukaazi granite. Thus, Cl/F ratio is interpreted to be very low in Kukaazi apatite since the source magma is deficient in halogen specifically chlorine. In this scenario, it can be inferred that the Cl/F ratios of Kukaazi apatite are most likely controlled by melt composition. According to Pan et al. (2016), the apatites constant Cl/F ratios equivalent to 0 from the granitic rocks, are indicative of no systematical variations during degassing. However, in the present study the Cl/F ratios of apatite are not equal to zero and exhibit variations. Hence, discrepancy in the Cl/F values of apatite can be attributed to variability of degassing which fractionated chlorine and fluorine (Warner et al., 1998). Experimental investigations reveal that F is preserved in the melt however, Cl is favorably partitioned in water rich phase (Mathez and Webster, 2005; Webster et al., 2009). If crystallization of apatite takes place from hydrous magma, it should contain appropriate Cl concentration because of water fugacity. In Fig. 5b, the negative correlation of F and Cl implies crystallization of Kukaazi apatite from hydrous parental magma and magmatic water contents with noticeable contents of Cl/F ratios can be promising for the development of ore deposits. Consequently, we propose that the fertile rocks may comprise apatite low Cl content contradicting with the finding of Xie et al. (2018), which demonstrates that the apatite crystals from the fertile rocks contain much higher Cl content. Our findings can be supported by plot of Eu/Eu* vs. Cl content (Fig. 10) which suggests that the rocks containing even low Cl concentration are mineralized. Therefore, it is worth stating that the apatite Cl/F ratios as well as Eu/Eu* vs. Cl content can be used as fingerprint and proxy for mineralized deposits.

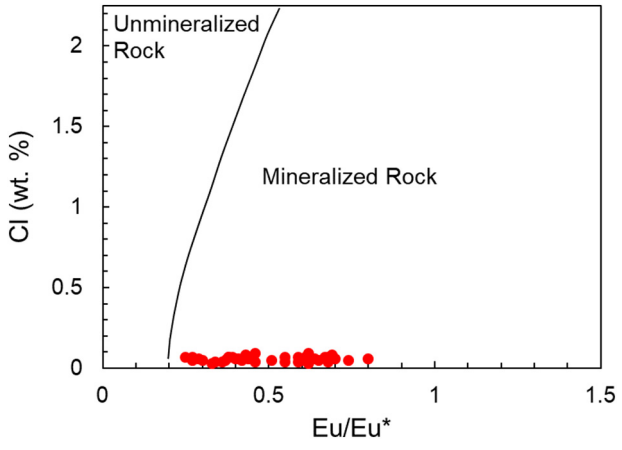

Fig. 10. Plot of Cl (wt%) vs. Eu/Eu* to discriminate mineralized and unmineralized rock. Fields are after Mao et al. (2016).

6.5. Kukaazi apatite as potential pointer of metallogenesis, mineralization and ore types

As stated above that the geochemistry of apatite particularly its trace elements and halogens normally reveal magmatic conditions. This, together with the characteristic that apatite is less prone to alteration process, which is considered as prime attribute of mineralized granites relative to amphibole, micas and feldspar, makes apatite a significant and vigorous tool for assessing the mineralization potential of Kukaazi granite. Additionally, its geochemical portrayal can be important to evaluate the degree of magmatic differentiation. Fig. 11a reveals obvious variation and positive correlation between F/Cl ratios and F contents which possibly can be an indication of magmatic fractionation/differentiation supported through silica content of whole rock ranging from 61.15 to 66.99 wt%; the calculated data for whole rock SiO_2 content in granites are from Y.H. Wang et al. (2013). This interpretation is parallel with the findings of Cao et al. (2012). Furthermore, negative correlation of Mn versus (Eu/Eu*) N also reflects degree of magmatic differentiation (Fig. 11b). The increase in fluorine content of apatite is primarily owing to fractionation (Nash, 1984). Likewise, the (La/Yb) N and δEu in apatite exhibits differentiation of rare earth elements (Fig. 12c, d); and moderate oxidized state of the magma during crystallization of apatite. Diverse natures of ore deposits are associated to discrete differentiated magma together with moderate oxidized state of magma, thus various kinds of deposits indicate different characters of Sr, δEu, Y, F and (La/Yb) N in apatite (Fig. 12). The magmatic apatite various geochemical characteristics are significant to distinguish their linked mineral deposits. Using apatite geochemistry and through interpretation of binary plots, we identified two types of ore deposits in Kukaazi area. The plot of F versus Sr indicates that Mo-W deposit of Kukaazi contains slightly higher fluorine comparative to copper deposits; however, copper deposit is distinguished by higher concentration of Sr in comparison to Mo-W deposit. On the contrary, apatite plot of Sr versus δEu displays that Mo-W deposit comprises lesser Sr and δEu value relative to copper deposit. Likewise, plot of (La/Yb) N versus Sr exhibits that Mo-W deposit has very low values of these comparative to copper deposits, and plotting of Y versus Sr indicates that Mo-W deposit is characterized by higher Y but lower content of Sr in contrast to copper deposits. Thus, in view of these findings, we can suggest that contents of Sr, δEu, Y, F and (La/Yb) N in apatite can be significant to typify the degree of differentiation and ore deposit varieties (Fig. 12).

7. Conclusions

Most important findings from this research can be summarized as follows:

(1) The apatite of Kukaazi deposit can be characterized as fluorapatite and based on its textural characteristics, fluorapatite nature and SiO_2-MnO plot, we can conclude that its magmatic apatite, significant to reflect the parental magma characteristics of Kukaazi granite.
(2) The apatite in the Kukaazi granite contains high fluorine contents, a right inclined distribution pattern with enrichment of light rare earth elements (LREE) comparative to heavy rare earth elements (HREE), and noticeably moderate negative Eu anomaly which is possibly resulting from plagioclase crystallization earlier than apatite. The observed concentrations of trace elements of apatite in Kukaazi granite are attributable to apatite and melt partition coefficients as well as the contents in the parental material. Additionally, higher Sr content in apatite comparative to host rock can be attributed to restricted feldspar crystallization or magmatic involvement from lower crustal or mantle source.
(3) Interpretation of negative correlation and variation of δCe and δEu in apatites of Kukaazi area exhibit significant character to

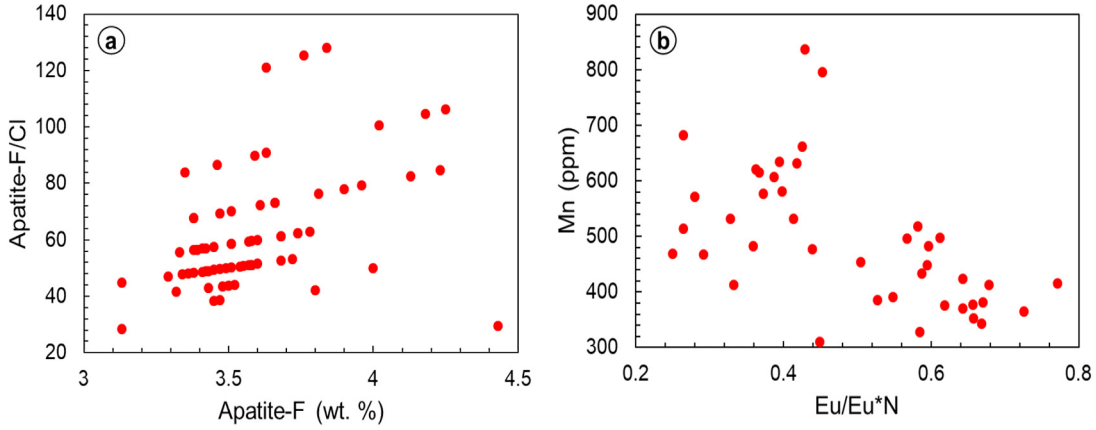

Fig. 11. Plots of (a) apatite F/Cl ratio vs. F (wt%); (b) apatite Mn (ppm) vs. Eu/Eu*.

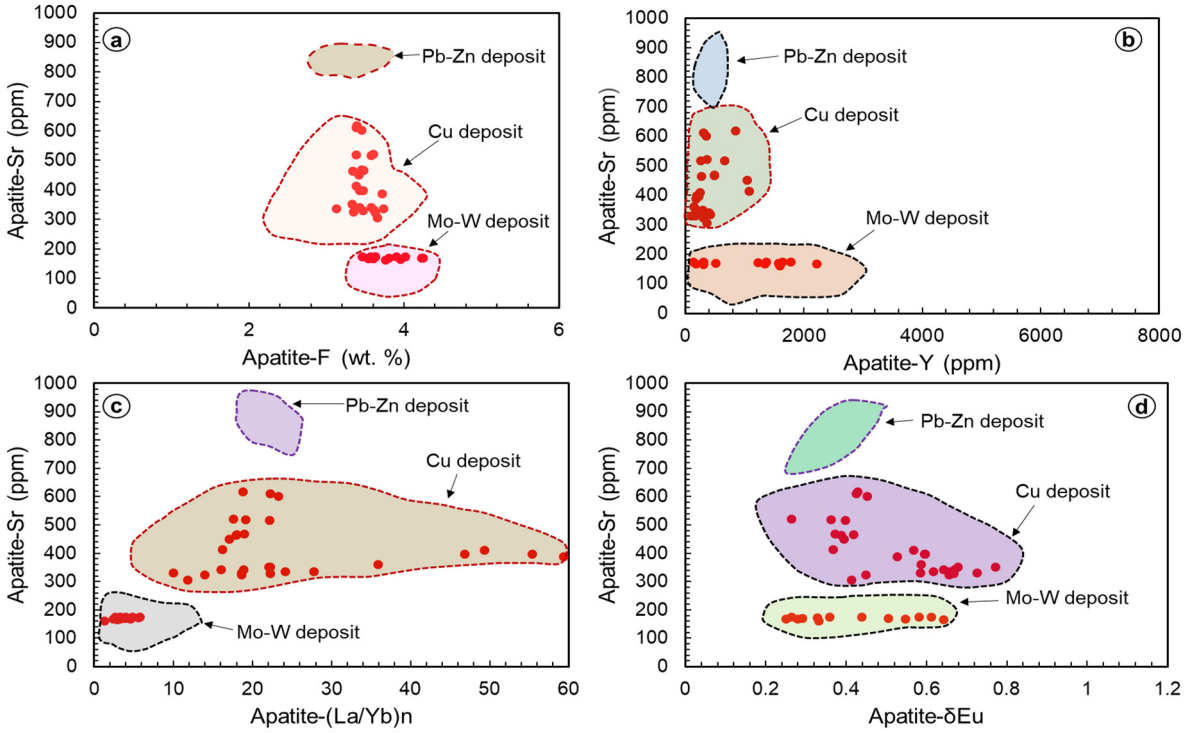

Fig. 12. Apatite discrimination plots from Kukaazi granites of Western Kunlun: (a) F (wt%) vs. Sr (ppm); (b) Y (ppm) vs. Sr (ppm); (c) (La/Yb) n vs. Sr (ppm); (d) δEu vs. Sr (ppm). The fields are after Cao et al. (2012).

characterize the nature of magma. The moderate negative Eu anomaly examined in the apatite implies that the parental magma of the Kukaazi granite have moderate oxidizing nature.

(4) The higher Sr/Y and Eu/Eu* ratios characterized Kukaazi pluton with adakitic affinity. We conclude that this fluorapatite which is not prone to alteration process, can be robust tool for recognizing the adakite plutons and preserves original Sr/Y and Eu/Eu* ratios in consequence of no impact of hydrothermal alteration.

(5) Apatite halogen composition is considered as vigorous tool to track content of magmatic volatiles and proxy for mineralization. Our results deduced low Cl/F ratio in the parental magma of Kukaazi pluton, attributable to source control and variation in the Cl/F values can be ascribed to variability of degassing. Low Cl, fairly high F and low Cl/F ratios implies that the parental magma of Kukaazi granite is depleted in chlorine and originated in consequence of partial melting of lower crust material. The negative correlation of F and Cl suggests crystallization of Kukaazi apatite from hydrous parental magma. In addition, apatite Eu/Eu* vs. Cl content can be used as fingerprint and proxy for ore deposits.

Acknowledgements

This work was funded by the Chinese NSF Projects (41673051, 41872097), the ARC Centre of Excellence-linking fund (P2A3). We wish to express our appreciation to David Cooke, Leonid Danyushevsky, Sarah Gilbert, Le-Jun Zhang, Wei Hong, and Qiu-Yue Huang from the University of Tasmania, for their laboratory assistances and fruitful discussion. Contributions of Zeng-Hua Li are productive and admirable for polishing the manuscript.

References

Aigner–Torres, M., Blundy, J., Ulmer, P., Pettke, T., 2007. Laser ablation ICPMS study of trace element partitioning between plagioclase and basaltic melts: an experimental approach. Contrib. Mineral. Petrol. 153, 647–667.

Ayers, J.C., Watson, E.B., 1991. Solubility of apatite, monazite, zircon and rutile in supercritical aqueous fluids with implications for subduction zone geochemistry. Philos.

Trans. R. Soc. London. A 335, 365–375.
Ayers, J.C., Watson, E.B., 1993. Apatite/fluid partitioning of rare earth elements and strontium: experimental results at 1.0 GPa and 1000 °C and application to models of fluid-rock interaction. Chem. Geol. 110, 299–314.
Belousova, E.A., Walters, S., Griffin, W.L., O'Reilly, S.Y., 2001. Trace-element signatures of apatites in granitoids from the Mt Isa Inlier, northwestern Queensland. Aust. J. Earth Sci. 48, 603–619.
Belousova, E.A., Griffin, W.L., O'Reilly, S.Y., Fisher, N.I., 2002. Apatite as an indicator mineral for mineral exploration: trace-element compositions and their relationship to host rock type. J. Geochem. Explor. 76, 45–69.
Bi, X.W., Cornell, D.H., Hu, R.Z., 2002. REE composition of primary and altered feldspar from the mineralized alteration zone of alkali-rich intrusive rocks, western Yunnan Province, China. Ore Geol. Rev. 19, 69–78.
Bonin, B., 1988. Peralkaline granites in Corsica: some petrological and geochemical constraints. Rendiconti della Società italiana di Mineralogia e Petrologia. 43, 281–306.
Bonyadi, Z., Davidson, G.J., Mehrabi, B., Meffre, S., Ghazban, F., 2011. Significance of apatite REE depletion and monazite inclusions in the brecciated Se–Chahun iron oxide–apatite deposit, Bafq district, Iran: Insights from paragenesis and geochemistry. Chem. Geol. 281, 253–269.
Bouzari, F., Hart, C.J.R., Barker, S., Bissig, T., 2011. Porphyry indicator minerals (PIMS): a new exploration tool for concealed deposits in south-central British Columbia. Geoscience BC Report. 17, 1–31.
Boyce, J.W., Liu, Y., Rossman, G.R., Guan, Y.B., Eiler, J.M., Stolper, E.M., Taylor, L.A., 2010. Lunar apatite with terrestrial volatile abundances. Nature 22, 466–470.
Boynton, W.V., 1984. Cosmochemistry of the Rare Earth Elements: Meteorite Studies. 2. Elsevier Science Publishing Company, Amsterdam, pp. 63–114.
Bruand, E., Fowler, M., Storey, C., Darling, J., 2017. Apatite trace element and isotope applications to petrogenesis and provenance. Am. Mineral. 102, 75–84.
Buick, I.S., Hermann, J., Maas, R., Gibson, R.L., 2007. The timing of subsolidus hydrothermal alteration in the central zone, Limpopo Belt (South Africa): constraints from titanite U–Pb geochronology and REE partitioning. Lithos 98, 97–117.
Candela, P.A., 1986. Toward a thermodynamic model for the halogens in magmatic systems: an application to melt-vapor-apatite equilibria. Chem. Geol. 57, 289–301.
Cao, M.J., Li, G.M., Qin, K.Z., Seitmuratova, E.Y., Liu, Y.S., 2012. Major and trace element characteristics of apatites in granitoids from central Kazakhstan: Implications for petrogenesis and mineralization. Resour. Geol. 62, 63–83.
Chakhmouradian, A.R., Reguir, E.P., Zaitsev, A.N., Couëslan, C., Xu, C., Kynický, J., Mumin, A.H., Yang, P., 2017. Apatite in carbonatitic rocks: compositional variation, zoning, element partitioning and petrogenetic significance. Lithos 274, 188–213.
Chen, W., Simonetti, A., 2014. Evidence for the multi-stage petrogenetic history of the Oka carbonatite complex (Québec, Canada) as recorded by perovskite and apatite. Minerals 4, 437–476.
Chen, L., Zhang, Y., 2018. In situ major, trace-elements and Sr-Nd isotopic compositions of apatite from the Luming porphyry Mo deposit, NE China: constraints on the petrogenetic metallogenic features. Ore Geol. Rev. 94, 93–103.
Chen, L., Yan, Z., Wang, Z.Q., Wang, K.M., 2017. Characteristics of apatite from 160~140 Ma Cu (Mo) and Mo (W) deposits in East Qinling. Acta Geol. Sin. 91, 1925–1942 (in Chinese with English abstract).
Chu, M.F., Wang, K.L., Griffin, W.L., Chung, S.L., O'Reilly, S.Y., Pearson, N.J., Iizuka, Y., 2009. Apatite composition: tracing petrogenetic processes in trans Himalayan granitoids. J. Petrol. 50, 1829–1855.
Creaser, R.A., Gray, C.M., 1992. Preserved initial $^{87}Sr/^{86}Sr$ in apatite from altered felsic igneous rocks: a case study from Middle Proterozoic of south Australia. Geochim. Cosmochim. Acta 56, 2789–2795.
Cui, J.T., Wang, J.C., Bian, X.W., Zhu, H.P., Yang, K.J., 2006. Geological characteristics of Early Paleozoic amphibolite and tonalite in northern Kangxiwar, West Kunlun, China and their zircon SHRIMP U–Pb dating. Geol. Bull. Chin. 25, 1441–1449 (in Chinese with English abstract).
Cui, J.T., Wang, J.C., Bian, X.W., Zhu, H.P., Luo, Q.Z., Yang, K.J., Wang, M.C., 2007. Zircon SHRIMP U-Pb dating of Early Paleozoic granite in the Menggubao-Pushou area on the northern side of Kangxiwar, West Kunlun. Geol. Bull. Chin. 26, 710–719 (in Chinese with English abstract).
Doherty, A.L., Webster, J.D., Goldoff, B.A., Piccoli, P.M., 2014. Partitioning behavior of chlorine and fluorine in felsic melt–fluid(s)–apatite systems at 50 MPa and 850–950 °C. Chem. Geol. 384, 94–111.
Drake, M.J., 1975. Oxidation state of europium as an indicator of oxygen fugacity. Geochim. Cosmochim. Acta 39, 55–64.
Ekstrom, T.K., 1972. The distribution of fluorine among some coexisting minerals. Contrib. Mineral. Petrol. 34, 192–200.
Fang, X.L., Wang, Y.Z., 1990. Preliminary discussion on Caledonian granites in Western Kunlun Mountains. Xinjiang Geol. 8, 153–158 (in Chinese with English abstract).
Farley, K., Stockli, D., 2002. (U-Th)/He dating of phosphates: apatite, monazite and xenotime. Rev. Mineral. Geochem. 48, 559–577.
Filiberto, J., Treiman, A.H., 2009. The effect of chlorine on the liquidus of basalt: first results and implications for basalt genesis on Mars and Earth. Chem. Geol. 263, 60–68.
Fujimaki, H., 1986. Partition coefficients of Hf, Zr and REE between zircon, apatite and liquid. Contrib. Mineral. Petrol. 94, 42–45.
Gleadow, A.J.W., Belton, D.X., Kohn, B.P., Brown, R.W., 2002. Fission track dating of phosphate minerals and the thermochronology of apatite. Rev. Mineral. Geochem. 48, 579–630.
Harlov, D.E., 2015. Apatite: a fingerprint for metasomatic processes. Elements 11, 171–176.
Harlov, D.E., Andersson, U.B., Förster, H.J., Nyström, J.O., Dulski, P., Broman, C., 2002. Apatite–monazite relations in the Kiirunavaara magnetite–apatite ore, northern Sweden. Chem. Geol. 191, 47–72.
Harris, A.C., Kamenetsky, V.S., White, N.C., Steele, D.A., 2004. Volatile phase separation in silicic magmas at Bajo de la Alumbrera porphyry Cu–Au deposit, NW Argentina. Resour. Geol. 54, 341–356.
Harrison, T.M., Watson, E.B., 1984. The behavior of apatite during crustal anatexis: Equilibrium and kinetic considerations. Geochim. Cosmochim. Acta 48, 1467–1477.
Harrison, T., Catlos, E., Montel, J., 2002. U-Th-Pb dating of phosphate minerals. Rev. Mineral. Geochem. 48, 524–558.
Hasebe, N., Barbarand, J., Jarvis, K., Carter, A., Hurford, A., 2004. Apatite fission-track chronometry using laser ablation ICP-MS. Chem. Geol. 207, 135–145.
Henerson, P., 1980. Rare earth element partition between sphene, apatite and other coexisting minerals at the Kangerdlugssuag Intrusion, East Greeland. Contrib. Mineral. Petrol. 72, 81–85.
Hovis, G., Harlov, D., Hahn, A., Seigert, H., 2007. Enthalpies and volumes of F-Cl mixing in fluorapatite–chlorapatite crystalline solutions. Geophys. Res. Abstr. 9, 1748.
Hsieh, P., Chen, C., Yang, H., Lee, C., 2008. Petrogenesis of the Nanling mountains granites from South China: constraints from systematic apatite geochemistry and whole-rock geochemical and Sr–Nd isotope compositions. J. Asian Earth Sci. 33, 428–451.
Hughes, J.M., Rakovan, J.F., 2015. Structurally robust, chemically diverse-apatite and apatite supergroup minerals. Elements 11, 165–170.
Imai, A., 2002. Metallogenesis of porphyry Cu deposits of the western Luzon arc, Philippines: K-Ar ages, SO_3 contents of microphenocrystic apatite and significance of intrusive rocks. Resour. Geol. 52, 147–161.
Imai, A., 2004. Variation of Cl and SO_3 contents of microphenocrystic apatite in intermediate to silicic igneous rocks of Cenozoic Japanese island arcs: implications for porphyry Cu metallogenesis in the western Pacific island arcs. Resour. Geol. 54, 357–372.
Ishihara, S., 1981. The granitoid series and mineralization. Econ. Geol. 75th Anniversary 458–484.
Jahnke, R.A., 1984. The synthesis and solubility of carbonate fluorapatite. Am. J. Sci. 284, 58–78.
Jia, R.Y., 2013. Petrogenesis and Tectonic Implications of Qiukesugranite Pluton and Its Enclaves in the Western Kunlun Orogen Belt, NW China (Dissertation for master's degree of Nanjing University). pp. 1–62.
Jiang, Y.H., Rui, X.J., He, J.R., Guo, K.Y., Yang, W.Z., 1999. Tectonic type of Caledonian granitoids and tectonic significance in the west Kunlun Mts. Acta Petrol. Sin. 15, 105–115 (in Chinese with English abstract).
Jiang, Y.H., Rui, X.J., Guo, K.Y., He, J.R., 2000. Tectonic environments of granitoids in the West Kunlun orogenic blet. Acta Geosci. Sin. 21, 23–25 (in Chinese with English abstract).
Klein, M., Stosch, H.G., Seck, H.A., 1997. Partitioning of high field–strength and rare–earth elements between amphibole and quartz–dioritic to tonalitic melts: an experimental study. Chem. Geol. 138, 257–271.
Korzhinskiy, M., 1981. Apatite solid solutions as indicators of the fugacity of HCl and HF in hydrothermal fluids. Geochem. Int. 3, 44–60.
Krneta, S., Ciobanu, C.L., Cook, N.J., Ehrig, K., Kontonikas-Charos, A., 2016. Apatite at Olympic Dam, South Australia: a petrogenetic tool. Lithos 262, 470–485.
Leng, C.B., Wang, Y.H., Zhang, X.C., Gao, J.F., Zhang, W., Xu, X.Y., 2018. Constraints of molybdenite Re–Os and scheelite Sm–Nd ages on mineralization time of the Kukaazi Pb–Zn–Cu–W deposit, Western Kunlun, NW China. Acta Geochim 37, 47–59.
Li, H., Hermann, J., 2015. Apatite as an indicator of fluid salinity: an experimental study of chlorine and fluorine partitioning in subducted sediments. Geochim. Cosmochim. Acta 166, 267–297.
Liu, J.P., Wang, H., Li, S.H., Tong, L.X., Ren, G.L., 2010. Geological and geochemical features and geochronology of the Kayizi porphyry molybdenum deposit in the northern belt of western Kunlun, NW China. Acta Petrol. Sin. 26, 3095–3105 (in Chinese with English abstract).
Liu, Y., Zhang, R.Q., Abuduwayiti, M., Wang, C., Zhang, S., Shen, C., Zhang, Z., He, M., Zhang, Y., Yang, X., 2016. SHRIMP U–Pb zircon ages, mineral compositions and geochemistry of placer nephrite in the Yurungkash and Karakash river deposits, west Kunlun, Xinjiang, northwest China: Implication for a magnesium skarn. Ore Geol. Rev. 72, 699–727.
London, D., Wolf, M.B., Morgan, V.I,.G.B., Garrido, M.G., 1999. Experimental silicate-phosphate equilibria in peraluminous granitic magmas, with a case study of Albuquerque Batholith at Tres Arroyos, Badajoz, Spain. J. Petrol. 40, 215–240.
Mao, M., Rukhlov, A.S., Rowins, S.M., Spence, J., Coogan, L.A., 2016. Apatite trace element compositions: a robust new tool for mineral exploration. Econ. Geol. 111, 1187–1222.
Marks, M.A., Wenzel, T., Whitehouse, M.J., Loose, M., Zack, T., Barth, M., Barth, M., Worgard, L., Krasz, V., Eby, G.N., Stosnach, H., Markl, G., 2012. The volatile inventory (F, Cl, Br, S, C) of magmatic apatite: an integrated analytical approach. Chem. Geol. 291, 241–255.
Mathez, E.A., Webster, J.D., 2005. Partitioning behavior of chlorine and fluorine in the system apatite–silicate melt–fluid. Geochim. Cosmochim. Acta 69, 1275–1286.
Mattern, F., Schneider, W., 2000. Suturing of the proto- and paleotethys oceans in the western Kunlun (Xinjiang, China). J. Asian Earth Sci. 18, 637–650.
Mattern, F., Schneider, W., Li, Y., Li, X., 1996. A traverse through the western Kunlun (Xinjiang, China): tentative geodynamic implications for the Paleozoic and Mesozoic. Geol. Rundsch. 85, 705–722.
McInnes, B.I.A., Farley, K.A., Sillitoe, R.H., Kohn, B.P.C., 1999. Application of apatite (U-Th)/He thermochronometry to the determination of the sense and amount of vertical fault displacement at the Chuquicamata porphyry copper deposit Chile. Econ. Geol. 94, 937–947.
Meng, J.Y., 2014. The Porphyry Copper-Polymetallic Deposit in Zhongdian, West Yunnan: Magmatism and Mineralization (PhD Thesis). China University of Geosciences,

Beijing.
Miles, A.J., Graham, C.M., Hawkesworth, C.J., Gillespie, M.R., Hinton, R.W., Bromiley, G.D., 2014. Apatite: a new redox proxy for silicic magmas. Geochim. Cosmochim. Acta 132, 101–119.
Mitchell, R., Chudy, T., McFarlane, C.R., Wu, F.Y., 2017. Trace element and isotopic composition of apatite in carbonatites from the Blue river area (British Columbia, Canada) and mineralogy of associated silicate rocks. Lithos 286, 75–91.
Munoz, J., 1984. F-OH and Cl-OH exchange in micas with applications to hydrothermal ore deposits. Rev. Mineral. Geochem. 13, 469–493.
Nagasawa, H., 1970. Rare earth concentrations in zircons and apatites and their host dacites and granites. Earth Planet. Sci. Lett. 9, 359–364.
Nash, W.P., 1984. Phosphate minerals in terrestrial igneous and metamorphic rocks. In: Nriaguand, J.O., Moore, P.B. (Eds.), Phosphate Minerals. Springer-Verlag, Berlin, pp. 215–241.
Omar, G., Johnson, K., Hickey, L., Robertson, P., Dawson, M., Barnosky, C., 1987. Fission-track dating of Haughton astrobleme and included biota, Devon Island, Canada. Science 237, 1603–1605.
Pan, Y.S., 1989. A preliminary study on the regionalization of the structures in the Kunlun Mountains region. J. Nat. Resour. 4, 196–203 (in Chinese with English abstract).
Pan, Y., Fleet, M.E., 2002. Compositions of the apatite group minerals: substitution mechanisms and controlling factors. Rev. Mineral. 48, 13–49.
Pan, Y.S., Wang, Y., Matte, P., Tapponnier, P., 1994. Tectonic evolution along the geo traverse from Yecheng to Shiquanhe. Acta Geosci. Sin. 68, 295–307 (in Chinese with English abstract).
Pan, L.C., Hu, R.Z., Wang, X.S., Bi, X.W., Zhu, J.J., Li, C., 2016. Apatite trace element and halogen compositions as petrogenetic–metallogenic indicators: examples from four granite plutons in the Sanjiang region, SW China. Lithos 254, 118–130.
Parat, F., Holtz, F., Streck, M., 2011. Sulfur–bearing magmatic accessory minerals. Rev. Mineral. Geochem. 73, 285–314.
Piccoli, P.M., Candela, P.A., 1994. Apatite in felsic rocks: a model for the estimation of initial halogen concentrations in the Bishop Tuff (Long Valley) and Tuolumne intrusive suite magmas. Amer. J. Sci. 294, 92–135.
Piccoli, P.M., Candela, P.A., 2002. Apatite in igneous systems. Rev. Mineral. Geochem. 48, 255–292.
Pichavant, M., Montel, J.M., Richard, L.R., 1992. Apatite solubility in peraluminous liquids: experimental data and an extension of the Harrison-Watson model. Geochim. Cosmochim. Acta 56, 3855–3861.
Pyle, J.M., Spear, F.S., Rudnick, R.L., McDonough, W.F., 2001. Monazite xenotime-garnet equilibrium in metapelites and a new monazite garnet thermometer. J. Petrol. 42, 2083–2107.
Roeder, P.L., Mac Arthur, D., Ma, X.P., Palmer, G.R., Mariano, A.N., 1987. Cathodoluminescence and microprobe study of rare earth elements in apatite. Amer. Miner. 72, 801–811.
Sallet, R., 2000. Fluorine as a tool in the petrogenesis of quartz bearing magmatic associations: applications of an improved F-OH biotite-apatite thermometer grid. Lithos 50, 241–253.
Schoene, B., Bowring, S., 2007. Determining accurate temperature-time paths from U-Pb thermochronology: an example from the Kaapvaal craton, southern Africa. Geochim. Cosmochim. Acta 71, 165–185.
Scott, J.A.J., Humphreys, M.C.S., Mather, T.A., Pyle, D.M., Stock, M.J., 2015. Insights into the behaviour of S, F and Cl at Santiaguito Volcano, Guatemala, from apatite and glass. Lithos 232, 375–394.
Sha, L.K., Chappell, B.W., 1999. Apatite chemical composition, determined by electron microprobe and laser-ablation inductively coupled plasma mass spectrometry, as a probe into granite petrogenesis. Geochim. Cosmochim. Acta 63, 3861–3881.
Spear, F.S., Pyle, J.M., 2002. Apatite, monazite and xenotime in metamorphic rocks. Rev. Mineral. Geochem. 48, 293–335.
Streck, M.J., Dilles, J.H., 1998. Sulfur evolution of oxidized arc magmas as recorded in apatite from a porphyry copper batholith. Geology 26, 523–526.
Sun, H.T., Li, C.J., Wu, H., Wang, H.J., Qi, S.J., Chen, G.M., Liu, Z.T., Gao, P., 2003. Introduction to the West Kunlun Metallogenic Province. Geological Publishing House, Beijing (in Chinese).
Tepper, J.H., Kuehner, S.M., 1999. Complex zoning in apatite from the Idaho batholith: a record of magma mixing and intracrystalline trace element diffusion. Amer. Miner. 84, 581–595.
Treloar, P.J., Colley, H., 1996. Variations in F and Cl contents in apatites from magnetite-apatite ores in northern Chile, and their ore-genetic implications. Mineral. Mag. 60, 285–301.
Van Hoose, A.E., Streck, M.J., Pallister, J.S., Wälle, M., 2013. Sulfur evolution of the 1991 Pinatubo magmas based on apatite. J. Volcanol. Geotherm. Res. 257, 72–89.
Wang, C., Liu, L., Che, Z.C., He, S.P., Li, R.S., Yang, W.Q., Cao, Y.T., Zhu, X.H., 2009. Zircon U–Pb and Hf isotopic from the east segment of Tiekelike tectonic belt: constrains on the timing of Precambrian basement at the southwestern margin of Tarim, China. Acta Geosci. Sin. 83, 1647–1656 (in Chinese with English abstract).
Wang, C., Liu, L., He, S.P., Yang, W.Q., Cao, Y.T., Zhu, X.H., Li, R.S., 2013a. Early Paleozoic magmatism in west Kunlun: Constraints from geochemical and zircon U–Pb–Hf isotopic studies of the Bulong granite. Chin. J. Geol. 48, 997–1014 (in Chinese with English abstract).
Wang, Y.H., Leng, C.B., Zhang, X.C., 2013b. A-preliminary study on elemental geochemistry and geochronology of intermediate acidic intrusive rocks from Kukaazi Pb–Zn–Cu–W polymetallic deposit, Yecheng County, Xinjiang. Bull. Mineral. Petrol. Geochem. 32, 736–745 (in Chinese with English abstract).
Warner, S., Martin, R.F., Abdel-Rahman, A.F.M., Doig, R., 1998. Apatite as a monitor of fractionation, degassing and metamorphism in the Sudbury igneous complex. Ontario. Canad. Mineral. 36, 981–999.
Wass, S.Y., Henderson, P., Elliott, C.J., 1980. Chemical homogeneity and metasomatism in the upper mantle: evidence from rare earth and other elements in apatite-rich xenoliths in basaltic nodules from eastern Australia. Philos. Trans. R. Soc. London. 297, 333–346.
Watson, E.B., 1980. Apatite and phosphorus in mantle source regions: an experimental study of apatite/melt equilibria at pressures to 25 Kbar. Earth Planet. Sci. Lett. 51, 322–335.
Watson, E.B., Green, T.H., 1981. Apatite/liquid partition coefficients for the rare earth elements and strontium. Earth Planet. Sci. Lett. 56, 405–421.
Webster, J.D., Piccoli, P.M., 2015. Magmatic apatite: a powerful, yet deceptive, mineral. Elements 11, 177–182.
Webster, J.D., Tappen, C.M., Mandeville, C.W., 2009. Partitioning behavior of chlorine and fluorine in the system apatite–melt–fluid. II: felsic silicate systems at 200 MPa. Geochim. Cosmochim. Acta 73, 559–581.
Williams–Jones, A.E., Heinrich, C.A., 2005. Vapor transport of metals and the formation of magmatic–hydrothermal ore deposits. Econ. Geol. 100, 1287–1312.
Wolf, M.B., London, D., 1994. Apatite dissolution into peraluminous haplogranite melt: an experimental study of solubilities and mechanisms. Geochim. Cosmochim. Acta 58, 4127–4145.
Xiao, W.J., Windley, B.F., Chen, H.L., Zhang, G.C., Li, J.L., 2002. Carboniferous-Triassic subduction and accretion in the western Kunlun, China: implications for the collisional and accretionary tectonics of the northern Tibetan Plateau. Geology 30, 295–298.
Xiao, X.C., Wang, J., Sun, L., Song, S.G., 2003. A further discussion of the Kudi ophiolite, west Kunlun, and its tectonic significance. Geol. Bull. China 22, 745–750 (in Chinese with English abstract).
Xiao, W.J., Windley, B.F., Liu, D.Y., Jian, P., Liu, C.Z., Yuan, C., Sun, M., 2005. Accretionary tectonics of the Western Kunlun Orogen, China: a Paleozoic–Early Mesozoic, long-lived active continental margin with implications for the growth of southern Eurasia. J. Geol. 113, 687–705.
Xie, F., Tang, J., Chen, Y., Lang, X., 2018. Apatite and zircon geochemistry of Jurassic porphyries in the Xiongcun district, southern Gangdese porphyry copper belt: implications for petrogenesis and mineralization. Ore Geol. Rev. 96, 98–114.
Xu, R.H., Zhang, Y.Q., Xie, Y.W., Chen, F.K., Arnaud, N., 1994. A-discovery of an Early Paleozoic tectono-magmatic belt in the northern part of west Kunlun Mountains. Sci. Geol. Sin. 29, 313–328 (in Chinese with English abstract).
Xu, Z.Q., Yang, J.S., Li, H.B., Ji, S.C., Zhang, Z.M., Liu, Y., 2011. On the tectonics of the India-Asia collision. Acta Geosci. Sin. 85, 1–33 (in Chinese with English abstract).
Xu, Z.Q., Dilek, Y., Cao, H., Robinson, P., Ma, C.Q., Li, H.Q., Jolivet, M., Roger, F., Chen, X.J., 2015. Paleo-Tethyan evolution of Tibet as recorded in the east Cimmerides and west Cathaysides. J. Asian Earth Sci. 105, 320–337.
Yin, A., Harrison, T.M., 2000. Geologic evolution of the Himalayan-Tibetan orogen. Annu. Rev. Earth Planet. Sci. 28, 211–280.
Yu, X.F., Sun, F.M., Li, B.L., Ding, Q.F., Chen, G.J., Ding, Z.J., Chen, J., Huo, L., 2011. Caledonian diagenetic and metallogenic events in Datong District in the western Kunlun: evidence from LA-ICP-MS zircon U–Pb dating and molybdenite Re-Os dating. Acta Petrol. Sin. 27, 1770–1778 (in Chinese with English abstract).
Yuan, C., Sun, M., Zhou, M.F., Zhou, H., Xiao, W.J., Li, J.L., 2002. Tectonic evolution of the West Kunlun: geochronologic and geochemical constraints from Kudi Granitoids. Int. Geol. Rev. 44, 653–669.
Yuan, C., Sun, M., Xiao, W.J., Zhou, H., Hou, Q.L., Li, J.L., 2003. Subduction polarity of the prototethys: insights from the Yirba pluton of the western Kunlun range, NW China. Acta Petrol. Sin. 19, 399–408 (in Chinese with English abstract).
Zeitler, P., Herczeg, A., McDougall, I., Honda, M., 1987. U-Th-He dating of apatite-a potential thermochronometer. Geochim. Cosmochim. Acta 51, 2865–2868.
Zhang, Y.Q., Xie, Y.W., 1989. A study on the Rb–Sr biotite isochron ages of the granitoid in the Sanshiliyingfang area of the Karakoram and Kunlun MTS, region. J. Nat. Resour. 4, 222–227.
Zhang, C.L., Yu, H.F., Shen, J.L., Dong, Y.G., Ye, H.M., Guo, K., 2004. Zircon SHRIMP age determination of the giant-crystal gabbro and basalt in Kuda, west Kunlun: dismembering of the Kuda ophiolite. Geol. Rev. 50, 639–643 (in Chinese with English abstract).
Zhang, C.L., Yu, H.F., Wang, A.G., Guo, K.Y., 2005. Dating of Triassic granites in the Western Kunlun Mountains and its tectonic significance. Acta Geosci. Sin. 79, 645–652 (in Chinese with English abstract).
Zhang, C.L., Lu, S.N., Yu, H.F., Ye, H., 2007. Tectonic evolution of the Western Kunlun orogenic belt in northern Qinghai-Tibet Plateau: evidence from zircon SHRIMP and LA-ICP-MS U–Pb geochronology. Sci. China Ser. D Earth Sci. 50, 825–835.
Zhang, C., Holtz, F., Ma, C., Wolff, P.E., Li, X., 2012. Tracing the evolution and distribution of F and Cl in plutonic systems from volatile-bearing minerals: a case study from the Liujiawa pluton (Dabie orogen, China). Contrib. Mineral. Petrol. 164, 859–879.
Zhang, X.C., Wang, Y.H., Leng, C.B., Zhang, W., Xu, L.L., Zhu, J.J., Chen, Y.W., 2014a. Geology, sulfur isotopes and scheelite Sm–Nd age of the Kukaazi Pb–Zn–(Cu–W) polymetallic deposit, Yecheng County, Xinjiang, China. Acta Geol. Sin. 88, 244–246.
Zhang, Z.W., Shen, N.P., Peng, J.T., Yang, X.R., Feng, G.Y., Yu, F., Zhou, L.J., Li, Y.J., Wu, C.Q., 2014b. Syndeposition and epigenetic modification of the strata-bound Pb–Zn–Cu deposits associated with carbonate rocks in western Kunlun, Xinjiang, China. Ore Geol. Rev. 62, 227–244.
Zhang, Y., Niu, Y.L., Hu, Y., Liu, J.J., Ye, L., Kong, J.J., Duan, M., 2015. The syncollisional granitoid magmatism and continental crust growth in the West Kunlun Orogen, China - evidence from geochronology and geochemistry of the Arkarz pluton. Lithos 245, 191–204.
Zhu, C., Sverjensky, D.A., 1992. F-Cl-OH partitioning between biotite and apatite. Geochim. Cosmochim. Acta 56, 3435–3467.